Author response to reviewer comments

We would like to thank Luca Greco and Georg Raimund Pirrung for their thorough review, time and constructive and very meaningful comments. Their input helped to improve the original manuscript.

We addressed all comments and reply to these point by point. First the comment is repeated (in italics), followed by an answer of the authors and if applicable the excerpt from the LaTeX-Diff file (framed), highlighting the changes. Line numbers in the comments refer to the discussion version and line numbers in the response to the LaTeX-Diff of the revised manuscript, which is also attached as a complete version.

Luca Greco, Reviewer #1

**Reviewer #1 general comment:**

0. **[Reviewer #1]** *As a general comment I found the paper quite long. I understand that the presented results are many and they require suitable comments and description. Nevertheless, I encourage the authors to try to make the paper more concise to avoid the reader getting confused by so many details. For example, some of the results could be included in a specific Appendix whilst only the most important ones are retained in the main text.*

   [Authors] We completely see the point here. We approached this such that we identified the major messages in our conclusions and which measurements respectively analysis are needed for our argumentation to get to these conclusions. We identified the time constant analysis of the hot wire signals to be not relevant to reach our conclusions and thus moved this part to the appendix as suggested.

Reviewer #1 specific comments:

1. **[Reviewer #1] Figure 2**: *although the description of the experimental setup is very clear, I suggest that the authors include a 3D sketch of it to replace Figure 2. This would greatly help the reader in getting a quick overview of the setup and of the instrumentation.*

   [Authors] Thank you for this comment. We added another perspective (top view) of the setup for an improved quick overview of the setup. With this view the position of the LDA probe head on the traverse is obvious as well as the spread of the measurement positions of the hot wire and LDA focus points. We considered a 3D CAD derived sketch, however stayed with a 2D representation and added a second perspective view as we found it more clear and easier/quicker to see the coordinate system orientation. See below the updated Fig. 2.

Figure 2. Sketch of the setup in the wind tunnel. View from (a) the side and (b) the top.
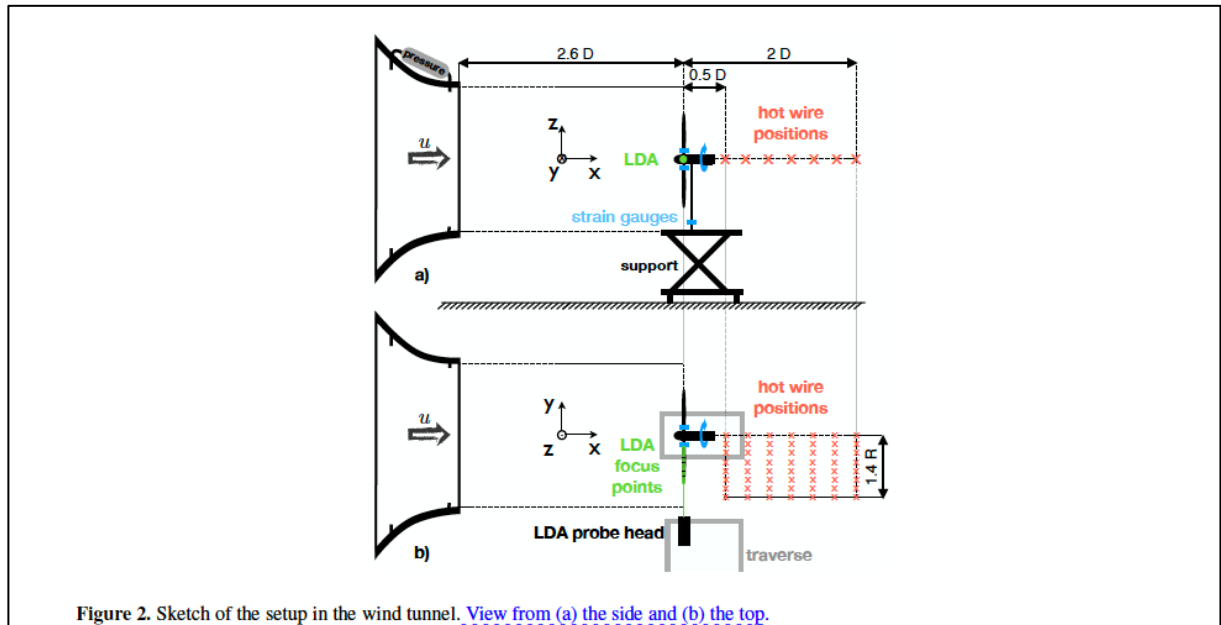
2. ***[Reviewer #1] line 113**: The authors state that the rotor blades are collectively pitched by 5.9°. In Figure 3 the pitch angle before imposing the step seems to be 5°. I suggest to include in the description of the rotor the blade pitch value corresponding to the considered operating conditions.*

[Authors] We added the actual pitch settings as suggested in the text (see line 117)

> The rotor blades are collectively pitched by $5.9°$ between $-0.9°$ and $5.0°$, within $0.070\,\mathrm{s}$, corresponding to about half a rotor revolution and half the reference time. The pitch step is from a low rotor load at a thrust coefficient $C_T = 0.48$ to a high load at $C_T = 0.90$ and vice versa, based on the strain gauge derived thrust. This corresponds to rotor effective inductions of
> 120 $a_{eff} = 0.14$, respectively $a_{eff} = 0.34$, based on the momentum theory relation ($C_T = 4a(1-a)$).

3. ***[Reviewer #1]** In **Section 2.1.3** the authors make reference to the work by Herràez (2018) for the description of the experimental technique used for the definition of the measurement line (the bisectrix of two rotor blades). For the sake of reading clarity, it would be beneficial to provide a bit more details supporting the choice of that line of measurements by clearly explaining the effect of each blade (bound circulation) and of the shed/trailed vorticity, and providing brief motivations for the limitations of this technique in catching the effect of trailed vorticity (which is very relevant close to tip and root of the blade). In this regard, I suggest also that the rotor plot in figure 4b should be made in 3D in order to better get the information about the point of view and of the direction of circulation on the blades. Finally, in Fig. 4A, the measured velocity components are not clear: is the tangential component a radial one? I believe that a 3D view of the rotor could help also in this regard.*

[Authors] This is a very helpful comment. The line of measurement is mainly defined by constraints from the LDA head mount options and the effect of the tower. We also elaborated further on the effect of each blade and the bound and trailed vorticity in the text. Figure 4 and caption was also modified to help understand the general concept quickly. In Fig. 4b firstly a coordinate system is introduced, and the orientation of the rotor is described in the caption. The vorticity circles are also modified according to the perspective to show the explicit direction. The vector orientations in Fig. 4a are also mentioned in the caption in terms of the coordinate system. The text additions (lines 139 - 149) and the revised Fig. 4 are shown below.

In Fig. 4 a the MoWiTO turbine is shown with the LDA laser beams and the probed axial (u_{ax}) and tangential (u_{ta}) velocity components at a specific radius. Alongside in Fig. 4 b, the concept of the counterbalancing of the bound circulation of the evenly loaded blades is sketched. ~~The tower~~ For the shown position the blade at the 9'o clock position has no influence on

140 the axial velocity on the indicated line of measurements. At that line the downwash of the blade ahead of the indicated line counteracts the upwash of the blade behind it and they cancel each other. The velocity at the line thus is only influenced by the wake induction. Herráez et al. (2018) argue, that the trailed vorticity especially at the tip might play a non-negligible role, as it cannot be captured well at the high distance between the measurement position and the blade tip. Therefore the method is less suited for the root and tip region of the blade.

145 Two constraints defined the line of LDA measurements. The first is the height range of the LDA probe head, which is from tower bottom to hub height. The second is to minimize the influence of the tower on the blade nearest to the tower for the measurements in the bisectrix of two blades. This led to a measurement line at the 3'o clock position. The tower does disturb the axial symmetry, however, based on an estimation of the tower effect with a dipole model as in Schepers (2012) the tower effect ~~at the measurement positions~~ on the 5'o clock blade position is considered negligible.
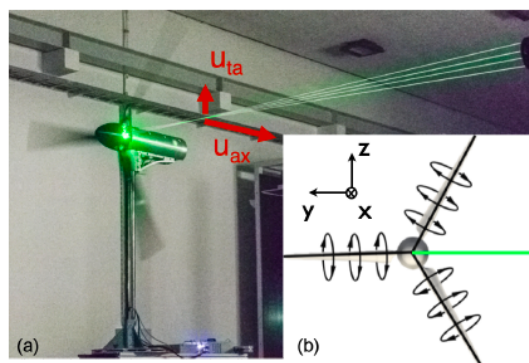

Figure 4. (a) ~~Rotating~~ Clockwise rotating MoWiTO 1.8 with 2D-LDA probing axial (along x-axis) and tangential velocity (along z-axis) components in the bisectrix of two blades. (b) Scheme of ~~principle of~~ counterbalancing bound circulation of the evenly loaded blades ~~in the bisectrix,~~ of front view of clockwise rotating rotor. The LDA measurement line is indicated in ~~red~~ green (adapted from Herráez et al. (2018)).

4. **[Reviewer #1]** *If I understood correctly, in **Section 2.1.3** the results of Fig. 5 should be comparable with the data in Herràez 2018. If so, it would be nice to plot the reference numerical data on top of the presented results. Moreover, in the cited paper the induced (perturbation) velocity reaches 0 value at the bisectrix of each pair of blades, i.e. at azimuth 60°, 180° and 300°. In the present results this is not verified (even if the mean value of the measurement, about 4 m/s, would be eliminated from the data) so the authors are invited to clarify these discrepancies. The operating conditions (wind speed, rpm) are not reported. In the paper by Herràez it is clear that the numerical data are obtained in a phase-locked way, i.e. considering blade 1 at 12 o'clock position and computing the velocity along a circle of radius r. Differently, here the authors seem to consider a fixed point whilst the blade is rotating. Please clarify this point.*

[Authors] This is a good point and we totally agree that our ~~original statement~~ statement was far fetched as you point out. We followed your suggestion and added the analytical solution according to the derivation by Herraez et al. 2018 to Fig. 5a (see below). The implementation and also the differences to the case presented in the Herraez et al. 2018 paper are outlined in Appendix A (lines 655-670). We further added the info that the shown measurement is from the steady high load operational point, that is defined priorly (line 151).

150 To obtain the values in the bisectrix, ~~we synchronised~~ the LDA system is synchronised with the MoWiTO data acquisition system. Measurements at ~~constant~~ the constant high load are plotted for one position of the axial and tangential probe over the azimuth angle ϕ_1 of the turbine in Fig. 5. The bisectrix values that are in a threshold of $\pm 3°$ are marked in red. ~~We identified~~

~~Note that the axial probe does look like the theoretical derivation of the signal in reference Herráez et al. (2018)~~

155 In Fig. 5 a also the analytical course seen by the axial probe according to Herráez et al. (2018) (see App. A), is presented and shows a good match to the measured signal. This good fit gives a high level of confidence on the applicability of the method to this experiment. For the tangential probe, data is missing around $-1.3\,\mathrm{ms}^{-1}$ and also at $2.3\,\mathrm{ms}^{-1}$ for the axial probe, which
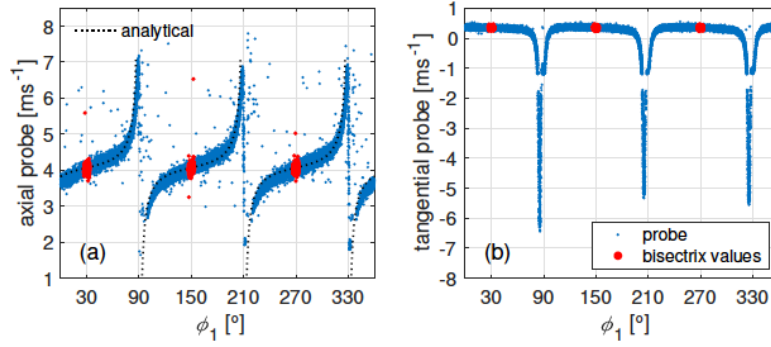

Figure 5. (a) Measurements of axial probe for high load case at a radius of $0.7\,R$ for 400 revolutions over azimuth angle ϕ_1 with marked data within the bisectrix threshold. $\phi_1 = 0°$ relates to the 12 o'clock position of blade 1. (b) Analogously for the tangential probe.

655 **Appendix A: Counterbalance of the blade induction at the bisectrix between consecutive blades**

The detailed derivation based on the theorem of Biot-Savart is given in Herráez et al. (2018) but the relevant formulas to produce the analytical solution in Fig. 5 a are given here.

Eq. (A11) of Herráez et al. (2018) is reproduced in Eq. (A1). The velocity induced by each of the N rotor blades (numbered $i \in [1, 2, ..., N]$) is given in dependance of the azimuth angle of the blade ψ_i, the azimuth angle of the sampling point β and the

660 coordinates along the blade spanwise direction l. The circulation along the blade span is given by $\Gamma_i(l)$ and the azimuth angle of all blades can be defined by $\psi_i = \psi_1 + (i-1)\Delta\psi$, where $\Delta\psi = \frac{2\pi}{N}$.

$$u_i(r) = \frac{1}{4\pi} \int_0^R \Gamma_i(l) \frac{r\sin(\psi_i - \beta)}{[r^2 + l^2 - 2lr\cos(\psi_i - \beta)]^{\frac{3}{2}}}\, \mathrm{d}l \tag{A1}$$

Herráez et al. (2018) use a phase lock of the rotor for the simulations and compute the velocity along a circle for a specific radius. For the PIV validation in Herráez et al. (2018) and the application in this paper a stationary probe is used and the

665 rotor position is varied. The circulation $\Gamma_i(l)$ is obtained from the lift distribution calculated in Eq. 9 by the Kutta–Joukowski theorem.

The analytical solution of the axial probe $u_{probe, analytical}$ in Fig. 5 a considers an axial velocity of $u_{ax} = 4ms^{-1}$ and the combined effect of all three blades according to Eq. (A2). Note that the Eq. (A1) has a singularity for the probe position and a blade element being at the exact same position, that are excluded from the plot (90°, 210° and 330°).

670 $$u_{probe, analytical}(r) = \sum_{i=1}^{N} u_i(r) + u_{ax}(r) \tag{A2}$$

5. *[Reviewer #1] Section 2.2: in the end of the paper the authors correctly state that the proposed methodology for the estimate of the dynamic inflow time constants can be very important for the enhancements of engineering models. From the presented analysis it is also clear that the synthesized time constants depend on several parameter such as the radial position, the pitch direction and (?) TSR. So it would be very interesting to include in the paper a brief discussion on how this methodology could be generalized to be used in an engineering model which must be applied to several load cases in the design of a wind turbine.*

[Authors] That is a good point. We added a paragraph at the end of Sect. 2.2 describing how the so obtained time constants can be used to assess the time constants of the Øye and new DTU dynamic inflow model and what the typical scaling parameters to size and operation are (lines 231-235).

> These time constants can be used for comparison and tuning of the time constants in the dynamic inflow engineering models of Øye (see Snel and Schepers (1995)), used in OpenFAST and GH Bladed, and the new DTU model (see Madsen et al. (2020)), used in HAWC2. The time constants of these engineering models are derived from simulations and parametrised to the turbine size and operational condition considering the relevant dynamic inflow time scaling factor $\frac{u_0}{R}$, the radial position and
> 235 the quasi-steady axial induction factor.

Using these three common scaling quantities we get time constants for two axial induction settings, that give a good span for the relevant induction settings and such are a good basis for validation of existing models (see also Berger et al. 2020 https://doi.org/10.1088/1742-6596/1618/5/052055). They are however not sufficient for development of new models. We added two sentences in the conclusions on a further planned experiment to increase this data basis and enable model development from experimental data (line645-650).

> Further investigations are recommended with ~~high-fidelity~~ high-fidelity models of induction effects, eg. FVWM or Actuator
> 645 Line CFD simulations to support the interpretation of the data ~~.~~ and improvement of models. Further planned steps to extend the understanding of the dynamic inflow process and enhance or develop models on the basis of this experimental setup are the generation of a wider database of pitch steps with varying parameters of inflow velocities, rotor speeds and rotor induction levels but also more realistic inflow conditions, including e.g. non-uniform inflow and gusts. With a wider database it can be tested if besides the axial induction, radial position and typical dynamic inflow time scaling factor $\frac{u_0}{R}$ further parameters have
> 650 a significant influence on the time constants, as e.g. the operating TSR, background turbulence or non-uniform inflow. Due to

6. *a [Reviewer #1] In Section 2.3 the authors explain that in the load reconstruction from induction measurements lift and drag coefficients are obtained by Xfoil. Has any correction to take into account for 3D effects been considered? It is well known that sectional loads are typically underestimated if purely 2D polars are used in the framework of BET/BEMT theories. My impression is that loads reconstruction could be improved by the use of 3D-corrected polars. For the NREL 5 MW rotor these are available in the report by NREL describing the turbine characteristics.*

[Authors] That is a very good point we originally did not consider. We implemented the quiet common model by Snel (line 250-252) on the lift polar to account for 3D effects. There is a slight effect of higher reconstructed thrust at the high load operational point reducing the mismatch to the strain gauge measured from -7% to -6%. The other load channels and the loads at the low load configuration stay constant.

> 250 by XFoil (see Drela (1989)). The ~~blade~~ lift polars are corrected for 3D effects, as lift coefficients on rotating blades can be significantly higher than for a stationary blade due to the effect of cross lows related to a stall delay. This effect is most relevant for the root airfoils and was corrected by the method by Snel et al. (1993). The blade segment width is Δr and c the chord

b [Reviewer #1] *In this section it is also mentioned that the model by Pirrung et al. 2017 is used to take into account unsteady airfoil aerodynamics. Even though the paper is cited correctly and easily found in the literature, for the sake of clarity it would be beneficial to add (here or in a devoted Appendix) the main details of this model. Finally, I did not understand the sentence on line 231 "The typical time lag....": maybe it is related to some aspects of the model by Pirrung? In any case I suggest to rephrase the sentence to clarify the role of the two mentioned time constants.*

[Authors] Thank you for this helpful comment. We see the point, that some more information on the uA model would be helpful already in this paper. Thus we reproduced the main model in Appendix B (lines 671-679).

We further clarified the sentence on the role of the two time constants (line 260-261)

Appendix B: Unsteady aerodynamics model

The uA model as described in detail in Pirrung et al. (2017) Sect. 2.3 is reproduced with slightly altered variable names. The model consists of two filter functions Eq. (B2, B3), which use the same time constant τ_{uA}^{j}, defined in Eq. (B1). The index

675 j denotes the time step and the index QS the quasi-steady solution. The time step of the simulation, respectively reconstruction, is defined by Δt. The effective angle of attack α_{eff}^{j}, that indcludes the uA effect, is obtained by Eq. (B4).

$$\tau_{uA}^{j} = \frac{c}{2u_{rel}^{j}} \tag{B1}$$

$$x_1^{j} = x_1^{j-1} \exp\left(-0.0455 \frac{\Delta t}{\tau_{uA}^{j}}\right) + \frac{1}{2}\left(\alpha_{QS}^{j} + \alpha_{QS}^{j-1}\right) 0.165 u_{rel}^{j}\left(1 - \exp\left(-0.0455 \frac{\Delta t}{\tau_{uA}^{j}}\right)\right) \tag{B2}$$

$$x_2^{j} = x_2^{j-1} \exp\left(-0.3 \frac{\Delta t}{\tau_{uA}^{j}}\right) + \frac{1}{2}\left(\alpha_{QS}^{j} + \alpha_{QS}^{j-1}\right) 0.335 u_{rel}^{j}\left(1 - \exp\left(-0.3 \frac{\Delta t}{\tau_{uA}^{j}}\right)\right) \tag{B3}$$

$$\alpha_{eff}^{j} = \frac{1}{2}\alpha_{QS}^{j} + \left(x_1^{j} + x_2^{j}\right)/u_{rel}^{j} \tag{B4}$$

---

260 influenced. The ~~typical time lag of this~~ main model is reproduced in App. B. The typical uA time constant which determines the lag of the angle of attack due to the uA effect is in the order of ~~c/v_{rel}~~ $\frac{c}{u_{rel}}$, whereas the typical time constant of the dynamic inflow effect is ~~R/u_0~~ $\frac{u_0}{R}$ and at least two magnitudes of size larger, as mentioned in Sect. 1. Reconstructed loads will be investigated with and without the uA model.

---

7. *[Reviewer #1]* *I did not fully understand the sentences from line 255 to 260. My understanding is that the aim is to determine a priori a range of variation of the AOA in unsteady (pitch step) conditions. Please rephrase the sentence to make it more clear.*

[Authors] Your understanding is correct. We added a sentence (line 286-287) to state the reason and give better context and tried to further improve the readability of the whole paragraph (line 284-292).

8. *[Reviewer #1] From the presented induction results it is evident that, in general, the time constants for model 1c and 2c depend on the considered radial position and on the pitch direction. Moreover, they also depend on the distance of the fitted measured velocity field from the rotor disk. Do the authors have any evidence that they also depend on the TSR? In order to use the 1c and 2c model within an engineering aerodynamic tool, it would be beneficial to have a relationship that somehow links the time constants used for fitting the induction to the operating conditions and the radial station. Moreover, do the author have any proposal on how to generalize the values of the synthesized constants in order to use them in different load cases (different pitch step but not only, for example yawed flow or floating wind turbines)? In other words, do the author think that the time constant values found in this analysis could be used for other turbines in other operating conditions?*

[Authors] This actually is a quite interesting comment. For this experimental campaign we only considered one TSR and two thrust levels. On that basis we thus cannot comment on a dependence on TSR. Until now the general understanding in the community is that the dynamic inflow effect depends on the thrust coefficient, respectively axial induction, the ratio of wind to radius (R/u_0) as well as radial position. In our view for a generalization only based on these measurements a wider range of pitch steps and conditions is needed. We emphasized that point at the end of the conclusions in an outlook (lines 642-647; Q5 above) and added these points to our list for future experiments on dynamic inflow. An existing model like the Øye model however, that uses the mentioned scaling parameters can be tuned based on these two relevant thrust settings.

9. *[Reviewer #1] Line 306: the authors highlight that for the tangential induction factor, a different value for t0 was used with respect to the axial case. Moreover, the variation of t0 along the radius is quite relevant. To my understanding, this radial variation was not present in the axial induction. Moreover, a different value of t0 is used also for the fitting of the velocity field further downstream (fig. 17). The author should comment on this difference and on the sensitivity of the time constants with respect to the choice of t0.*

[Authors] This is a valid point. For quantities with an overshoot, like the tangential induction such changes might have a relevant effect on the fitted time constants. For this specific case we ran the fitting again with the strictly fixed t_0 to the end of the pitch step and compared the results. This led to a reduction in the number of the valid fits by 1/3, however for the rest of the measurement points similar results were obtained. We added this in the text (line 351-354) and also Fig. 14.
For the hot wire time constant fit (that was moved to the Appendix C) we also sharpened the text to better explain the approach to obtain the start point of the time constant fit (line 681-685).
For the axial induction that does not show an overshoot we found no relevant effect of such small changes in the starting point of the fit.
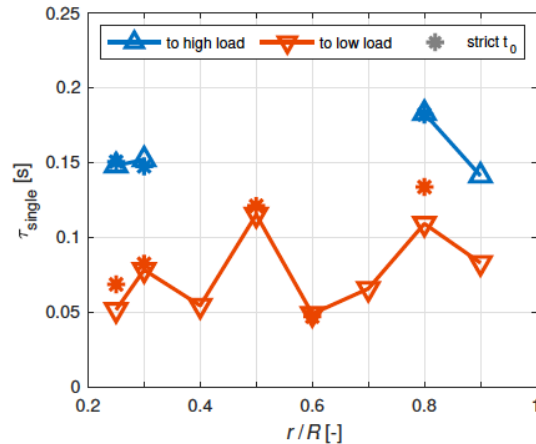
Figure 14. One time constant model fit of τ_{single} to the tangential wake induction over the radius for both pitch directions.

The influence of the small allowed shift in the start of the fit is also investigated. For a strict starting point of the fit at t_0, shown in Fig. 14 as stars, the set criterion of overshoot to noise is fulfilled for only three radii for the step to high load and five radii for the step to low load. For the available radii however there are only negligible differences to the shown fit in comparison to the observed spread.

355 ### 3.2 Wake results

The 1c model fit is applied to the hot wire signal shown in Fig. 17. The fit does start at t_0, which is defined at the point where the velocity has adjusted by 28% to the new equilibrium. This definition is less accurate than the end of the pitch step, as for the axial induction transients. However no direct fitting start time can be defined and this value is based on the mean value the axial inductions have adjusted during the pitch step. The aim of this definition is to make the time constants comparable to 685 these time constants of the axial wake induction.

10. *[Reviewer #1] Figure 17: might the drop in velocity at 0.2 R before the new equilibrium somehow be explained by the effect of the nacelle? Which is the radius of the nacelle?*

[Authors] The nacelle has a radius of 0.1R. We do not expect a relevant contribution from the nacelle wake at 0.2R (line 391-392).

both shown distances. The effect of the nacelle is assessed as unlikely to be the reason for this structure, as the nacelle only has a radius of $0.1\,R$. At the radius of $0.6\,R$ the signal decays exponentially. At 1 R the signal increases quickly to a peak at nearly free stream velocity before decreasing exponentially to the new steady value. The signals at $0.5\,D$ behind the turbine for the 395 two higher radii, $0.6\,R$ and $1\,R$, show a better fit with the exponential decay function. For the farther distance at $1.5\,D$ the hot

11. *[Reviewer #1] Figure 19: The caption is not clear (as well as the text on line 368). In particular I did not understand the definition of the wake ramp. Maybe a sketch could help in this regard.*

[Authors] Thank you for pointing out this unclear description. In a first step we changed the name of the wake ramp to wake front, for the analogy of a weather front. We changed the text for the introduction extensively as shown below. The general definition is sharpened in lines 389-390. The approach is reworked and extended in lines 406-421. The shortened caption is also shown (note that it is now Fig 18 due to a rearrangement before in the text and therefore the LaTeX-Diff highlighting did not work here, indicating everything in the caption as new).

For the radius at 0.6 R a vertical line, called ~~wake ramp, is drawn at~~ a wake front, marks a characteristic t_1 of the exponential

390 decay, where the signal has adapted by 50% to the new equilibrium value. For the radius of $0.2\,R$ the velocity transient shows

---

In the next step, ~~we analyse the wake ramp velocity~~ the wake front velocity is analysed to measure how fast the transition point (the wake ~~ramp~~front) between the old wake and the new wake ~~does convect. We define it as the velocity this wake ramp travels~~ convects. This wake front can be thought of as being similar to a weather front. We define the wake front velocity by the time this characteristic wake front needs to travel from one considered downstream position to the next. So exemplarily

410 in Fig. 17 at $0.6\,R$ ~~we do have the wake ramp~~ there is the wake front for $0.5\,D$ at $\underset{ramp,0.5D}{t} = 0.20\,s$ $t_{\text{front},0.5D} = 0.20\,\text{s}$ and for $1.5\,D$ at $\underset{ramp,1.5D}{t} = 0.56\,s$ $t_{\text{front},1.5D} = 0.56\,\text{s}$. Within this time difference, the wake ~~ramp~~front thus has travelled by $1\,D$, giving a mean wake ~~ramp~~front velocity between these downstream distances.

In Fig. 18, this wake ~~ramp~~front velocity is shown for both pitch directions, normalised by the free stream velocity. ~~Velocity of the wake ramp, defined by the mid point of the swept area weighted mean of the radii $0.4\,R$, $0.6\,R$ and $0.8\,R$, for both pitch~~

415 ~~directions, normalised by the free wind velocity. For orientation also the theoretical normalised wind velocity in the rotor plane~~

~~(1-a) and in far wake (1-2a), based on the measured thrust coefficient, are indicated for both steady states. The~~ The wake front velocity is obtained by considering a mean value of the hot wire positions at the radii of $0.4\,R$, $0.6\,R$ and $0.8\,R$~~were considered and a swept area-weighted mean, considering an annulus of~~. These signals were weighted based on their position with the conservation of mass in mind. For that each position was attributed an annulus reaching $\pm\,0.1\,R$ ~~for each radius, was used~~.

420 from the radius of the position. This mean velocity signal at the different downstream distances, which is used to obtain the wake front velocity, represents in this definition ($0.3\,R$ to $0.9\,R$) the major part of the swept area of the rotor. Thus between
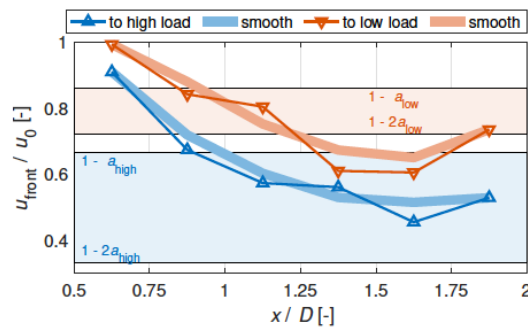

Figure 18. Velocity of the wake front for both pitch directions, normalised by the free wind velocity. For orientation also the theoretical normalised wind velocity in the rotor plane $(1-a)$ and in the far wake $(1-2a)$, based on the measured thrust coefficient, are indicated for both steady states.

---

12. ***[Reviewer #1] Section 3.3****: the paper includes several results. I don't think that in this section the (SG-no corr) results are really necessary as all the other ways of computing loads presented in this section do not include the mentioned correction.*

    [Authors] In the context the figure is described we completely agree and consequently removed that line from the plot as suggested.

13. ***[Reviewer #1] Line 390-391****: I did not fully understand this statement.*

    [Authors] We reworked the formulation of that sentence to make the statement more clear (line 445-448).

---

445 The slight overprediction of reconstructed loads for the M_{flap} and M_{aero} on the one hand and the underprediction of F_{thrust} ~~on a higher weighting of the higher radii~~for is attributed to a higher influence of the larger radii. For the first two signals ~~than for the~~ the blade acts as a lever arm for the sectional forces, thus giving them a higher weighting. In contrast the sectional forces are added without considering a lever arm for F_{thrust}~~signal~~.

14. **[Reviewer #1] Line 394-395**: *as already pointed out in my previous comments, might the use of the 2D polars instead of the 3D corrected one form an explanation for the deviation of LDA recon loads with respect to the strain gauges measurements? Moreover, at the end of the discussion the authors state that the main driver for the observed differences between reconstructed loads and SG measurements are the structural interactions. I suggest to investigate also the effect of 3D flow phenomena that are not fully included when using purely 2D polars.*

[Authors] As also put in the answer to question 6a in slightly more detail we now consider 3D effects for the lift polars and achieved a slight improvement for the reconstructed thrust at the high load level.

The observed differences you refer to in the text are the dynamic differences, so mainly the overshoot and time constant. Here especially the mismatch in the thrust overshoot can be related to the oscillation of the tower after the pitch step, that we could not completely filter out. For future experiments we will consider an accelerometer in the nacelle to consider these inertial forces, however the necessity of such a sensor is one of the lessons learned from this experimental campaign. Also the flexibility of the blades (very stiff but not perfectly stiff) and drivetrain add uncertainty to these highly dynamic experimental measurement.

15. **[Reviewer #1] Line 408-416:** *the theoretical procedure described in these lines to obtained the results in Fig. 23 is not clear to me. Please rephrase the paragraph for the sake of clarity.*

[Authors] Thank you for this hint. We rephrased that paragraph to increase the clarity. The reworked paragraph is shown below in (lines 465-475)

465   ~~The theoretical maximum overshoot~~ In order to assess the reasons for the differences in load overshoot it is of interest to investigate the theoretical maximum load overshoot when changing from one operational point to the other. This can be estimated based on the steady ~~induction measurements~~ states of the operational points and the theoretical dynamic maximum and minimum angle of attack distribution, as was ~~presented~~ introduced in Fig. 8 ~~, is investigated~~. The steady integral loads for high and low load are reconstructed as before for Fig. 19. ~~The maximum load overshoots are obtained by using~~ For the
470   maximum and minimum load the maximum and minimum dynamic angle of attack ~~distribution with the~~ distributions are used. The inflow to the segments is however defined by the inductions for the steady state just before the pitch step ~~, so an~~. An infinitely fast pitch step is assumed ~~and no~~, where the geometrical change of the blade pitch already happened, but the flow did not start to adapt. This apporach neglects uA effects that showed to reduce the overshoot ~~, are considered~~. The derived theoretical maximum amount of overshoot based on the difference of maximum, respectively minimum load and the following
475   steady load is plotted in Fig. 22. A clear difference can be seen between the pitch directions for the axial loads M_{flap} and

16. **[Reviewer #1] Line 453**: *it would be nice (not only here but in general in the discussion of the results) to indicate the percentage radial variation of t_slow and t_fast because the have very different magnitude and from the plot is not immediately evident.*

[Authors] We implemented that good point within the results (line 324-325 & 328-330) and discussion (line 514-517) section. Looking at these values we also slightly updated the conclusions (line 629-631).

The fitted τ_{fast} is high near the root for both pitch directions. For the step to high load τ_{fast} decreases from the root to $0.4\,R$, after which there is ~~a slight~~ an increase again (ignoring an outlier at $0.8\,R$). From $0.5\,R$ to $0.9\,R$ τ_{fast} increases by 67%.

325 For the step to low load τ_{fast} has ~~nearly~~ more constant values from $0.5\,R$ to $0.9\,R$, decreasing by 14%. Hence τ_{fast} is ~~shorter~~ smaller for the negative load step, for radii larger than $0.5\,R$, which represents 75% of the rotor swept area.

Values of τ_{slow} are slightly higher for the step to high load and show more variation than in the prior fit with $k = k_{\text{free}}$ ratio. There is a slight radial trend to higher values, with an increase in τ_{slow} from $0.3\,R$ to $0.9\,R$ by 11%. For the step to low load also more variation is apparent and a slight radial trend towards lower values is indicated, with a decrease in τ_{slow} from $0.3\,R$

330 to $0.9\,R$ by 16%. Taking the mean value over radius, the slow time constant for the step to low load is about 28% lower.

---

510 VI experiment, Sørensen and Madsen (2006) also saw this high τ_{fast} values at the root nearest radius of $0.3\,R$ for the step to low load, but not for the step to high load. In ~~our~~ the present and the phase VI experiment, this high τ_{fast} near the root is of the order of τ_{slow}. In ~~our~~ the present experiment, there is a ~~slight~~ difference in the τ_{fast} between pitch directions, with lower values for the step to low load from $0.5\,R$ to the tip. This difference between the pitch directions is not seen by Sørensen and Madsen (2006). Furthermore a radial dependance can also be seen from the mid of the blade towards the tip with an increase

515 for the step to high load (67%) and a slight decrease for the step to low load (−14%).

For τ_{slow}, a very slight radial dependency can be seen for the fit with k_{fix}, with slightly increasing values (11%) towards the tip for the step to high load and slightly decreasing values (−16%) for the step to low load, similar to the fit of τ_{single}.

---

model is more suited than a one time constant model to describe the behaviour of the axial induction for such a pitch step. The fast time constant of this model, representing the near wake influence, has a strong radial dependency near the root, ~~however not~~ and clear respectively slight dependency in the mid and tip region ~~, where it approaches constant values towards the outer~~

630 ~~part of the blade~~ for the step to high, respectively low load. The slow time constant, related to the close far wake, shows a slight decrease towards the outer part for the step to low load and a slight increase for the step to high load. The overshooting

---

Reviewer #1 technical corrections:

17. *[Reviewer #1]* *Throughout the paper large use of personal forms (like "we", "us", "our"...) is made. I find the impersonal forms to be more appropriate for a scientific paper. Please revise the whole manuscript taking care of this aspect.*

    [Authors] We changed the vast majority of these points to an impersonal form and only left this personal form at single instances where an opinion or presumption was stated.

18. *[Reviewer #1]* *In the abstract and in the introduction both present and past tenses are used when referring to literature results and also presented results: please make a coherent choice. I would suggest to use always the present tense.*

    [Authors] Thank you for pointing this out. We changed all to present tense as suggested.

19. *[Reviewer #1]* *line 84: pitching speed should be indicated in rad/s*

    [Authors] We added the pitching speed in rad/s.

20. *[Reviewer #1]* *line 130: "blades induction"*

    [Authors] We changed this according to the suggestion.

21. *[Reviewer #1]* *line 236: replace "along" with "with" and "from" with "described in".*

[**Authors**] We changed this according to the suggestion.

22. [**Reviewer #1**] *line 248: "low load case shows"*

[**Authors**] We changed this according to the suggestion.

23. [**Reviewer #1**] *line 292: replace "shorter" with "smaller"*

[**Authors**] We changed this according to the suggestion.

24. [**Reviewer #1**] *line 299: symbol t_fit was never defined before this point*

[**Authors**] We looked this up and actually the variable t_{fit} is introduced in line 205 along the method of the fitting procedure in Sect. 2.2.

25. [**Reviewer #1**] *line 525: replace "adopt" with "adapt"*

[**Authors**] We changed this according to the suggestion.

Georg Raimund Pirrung, Reviewer #2:

Reviewer #2 minor comments:

26. [**Reviewer #2**] *I think the angle 'theta' is not consistent between Equation (3) and Equations (11) and (12). In Equation (3) it is the sum of twist and pitch, and in Equations 11 and 12 it seems to be the inflow angle.*

[**Authors**] Thank you for pointing this out to us. You are completely right. We changed the variable in Eq. (3) for the sum of pitch and twist to 'gamma'.

27. [**Reviewer #2**] *Figure 11: I suggest to remove the irrelevant time constant tau_fast where k_free=1*

[**Authors**] That is a good idea. We implemented it according to your suggestion in the Fig. 11 and mentioned it in the text (line 312)

> 310   In Fig. 11, the three fitting parameters of the 2c model are presented. In the top row, the three fitted variables $k = k_{\text{free}}$, τ_{fast} and τ_{slow} are plotted over the radius. Near the root at $0.25\,R$ the k value for both pitch directions has a value of 1 respectively nearly 1, indicating no contribution from τ_{fast}, which consequently is also not plotted for these radii. For radii up to $0.5\,R$

28. [**Reviewer #2**] *Figure 16: It could be made a bit more clear what is actually shown in the figure. If I understand it correctly it is abs((u-u_0)/u_0)*

[**Authors**] Thank you for this comment. We added a sentence to clarify this point (line 373-375).

> steady state in Fig. 16. The normalised difference is defined as $\Delta u/u_0$, with $\Delta u = u_t - u_\infty$, where u_t is the velocity at the respective time at a measurement position and u_∞ the velocity at the same point at the new steady condition after the pitch
> 375   step. Therefore, a value of 0.5 means that the wake has to adapt by $0.5\,u_0$ to reach the new equilibrium. The starting conditions

29. **[Reviewer #2]** *Page 22 line 395 'High deviations are seen for Fthrust between strain gauge measurement and reconstructed loads, especially with the uA model, but also without the model, for both pitch directions.' Was the airfoil data 3D corrected? Without 3D correction the aerodynamics at the inboard sections might be inaccurately predicted by the load reconstruction procedure. This effect would be less visible on flapwise blade root moment and torque due to the short moment arms at the root section.*

[Authors] That is a good point. As also written in the answers to question 6a and 14 of the first reviewer we originally did not consider 3D corrected polars. Now we corrected our lift polars with the model proposed by Snel. We do achieve a slightly better match of the thrust at the high load case as you assumed. However there still is some relevant mismatch. We suspect that also the low Reynolds number polars with XFoil (especially those at the root which are at Re 60e3 at 0.2R; The airfoil is a low Re airfoil with low camber, but with 16% relative thickness rather thick for a model turbine) have relevant uncertainties and might lead to a further underprediction of the actual lift forces. Along this line also laminar separation bubbles at this root near stations, that can increase the local lift significantly, are possible. Such a reattaching bubble near the leading edge at the suction side is indicated by a high level of vorticity at a similar operational point at 0.25 R in a PIV measurement of the exact turbine with these blades for an angle of attack of 13° (published only in a presentation https://zenodo.org/record/3955740#.YURSMS221pQ slide 26 top left). We have added this suspicion to the text (line 585-587).

> For the steady equilibrium~~states, the quantitative~~, the comparison between the strain gauge measurements and the recon-
> structed loads (see Fig. 20) yields in generally good agreement, apart from the thrust at low load~~, which we suspect to be~~
> 585 ~~connected with the airfoil polars, especially at~~. Especially the here relevant high angle of attack region for the root air-
> foil is suspected to have uncertainties related to the low Reynolds number and possible laminar separation bubbles that can
> significantly increase the local lift.

Reviewer #2 small comments:

30. **[Reviewer #2]** *'tower bottom' bending moment is probably more frequently used than 'tower foot'*

[Authors] We implemented the change as suggested throughout the manuscript.

31. **[Reviewer #2]** *Page 10 line 230 'as a time lag on the angle of attack alpha'. You might add 'and has been extended to take the effect of camber into account'.*

[Authors] We implemented the addition also considering a reformulation suggested in question 6b (line 257-259)

> given in detail in Pirrung et al. (2017) is used. This is the inviscid part of the unsteady aerodynamics model by Hansen et al.
> (2004), which treats the shed vorticity effects due to fast angle of attack changes as a time lag on the angle of attack α and

> has been extended to take the effect of camber into account. Thus, the magnitude and direction of the aerodynamic forces are
> 260 influenced. The ~~typical time lag of this~~ main model is reproduced in App. B. The typical uA time constant which determines
> the lag of the angle of attack due to the uA effect is in the order of ~~c/v_{rel}~~ c/u_{rel}, whereas the typical time constant of the
> dynamic inflow effect is R/u_0 and at least two magnitudes of size larger, as mentioned in Sect. 1. Reconstructed loads will be
> investigated with and without the uA model.

32. **[Reviewer #2]** *Page 10 line 239 'unsteady aerodynamics model' -> unsteady airfoil aerodynamics model'*

    [Authors] We implemented the change as suggested.

33. **[Reviewer #2]** *Page 13 line 285 'influnece' -> influence*

    [Authors] We corrected this typo.

34. **[Reviewer #2]** *Page 23 line 400 'the normalised overshoot for the Mflap and Fthrust is similar per pitch direction, whereas the overshoot in Maero is 3 to 4.5 times higher'. I believe this is because the dynamic inflow effect causes the inflow angle and angle of attack to lag behind the quasi steady value. The thrust and the flapwise moment feel the effect mainly due to a change in magnitude of the lift force (due to the lag of the angle of attack), while the torque feels this change in magnitude and also the change in the projection of the lift force in the in-plane direction due to the lag of the inflow angle (Equation 12). Because the thrust force is determined using the cosine of the inflow angle (Equation 11), the effect of the inflow angle lag is much smaller there.*

    [Authors] Thank you for this excellent comment. We have added this argumentation closely based on your text in the discussion of the load overshoot (line 596-601)

    > The higher relative overshoot of the torque by a factor of 3 to 4.5 compared to the flapwise blade root bending moment and the rotor thrust can be related to the lag in inflow angle and thus angle of attack behind the quasi steady value. M_{flap} and F_{thrust} feel the effect mainly due to the change in the magnitude of the lift force, while M_{aero} feels the change in magnitude

    > and also the change of the projection of the lift force in the tangential direction due to the lag of the inflow angle (see Eq. 12).
    > 600 Because the F_{thrust} and mostly also M_{flap} are determined by the cosine of the inflow angle (see Eq. 11), the effect of the inflow angle lag is much smaller here.

35. **[Reviewer #2]** *Page 28 line 563 'by the shed vortex from the tip due to the fast change in trailed vorticity'. In the literature, sometimes 'shed vorticity' is used to describe vorticity that is parallel to the span, and 'trailed vorticity' to describe vorticity that is perpendicular to the span. Maybe you could instead write 'by the tip vortex due to the fast change in trailed vorticity'*

    [Authors] Thank your for making us aware of this unclear description. We have changed the sentence as proposed (line 638).

    > We assume that the dynamic inflow effect in this near wake is governed by the ~~shed vortex from the tip~~ tip vortex due to the
    > fast change in trailed vorticity. These vortices travel at such high velocities. Another finding is that the initial decay of the
    > 640 axial inductions during the pitch step is similar for both pitch directions. ~~We further identified~~ Furthermore, the aerodynamic

Experimental analysis of radially resolved dynamic inflow effects due to pitch steps

Frederik Berger[1], David Onnen[1], J. Gerard Schepers[2,3], and Martin Kühn[1]

[1]ForWind - Center for Wind Energy Research, University of Oldenburg, Institute of Physics, Küpkersweg 70, 26127 Oldenburg, Germany
[2]TNO Energy Transition, Petten,1755 LE, The Netherlands
[3]Hanze University of Applied Sciences, Groningen, 9747 AS, The Netherlands

Correspondence: Frederik Berger (frederik.berger@uol.de)

Abstract. The dynamic inflow effect denotes the unsteady aerodynamic response to fast changes in rotor loading due to a gradual adaption of the wake. This does lead to load overshoots. The objective of the paper was to increase the understanding of that effect based on pitch step experiments on a 1.8 m diameter model wind turbine, which ~~we~~ are performed in the large open jet wind tunnel of ForWind - University of Oldenburg. ~~We measured the~~ The flow in the rotor plane is measured with a 2D Laser Doppler Anemometer and ~~were able to extract~~ the dynamic wake induction factor transients in axial and tangential direction are extracted. Further, integral load measurements with strain gauges and hot wire measurements in the near and close far wake ~~were~~ are performed. ~~Our~~ The results show a clear gradual decay of the axial induction factors after a pitch step, giving the first direct experimental evidence of dynamic inflow due to pitch steps. ~~We fitted two engineering models~~ Two engineering models are fitted to the induction factor transients to further investigate the relevant time constants of the dynamic inflow process. ~~We discussed the~~ The radial dependency of the axial induction time constants as well as the dependency on the pitch direction ~~. We~~ is discussed. It is confirmed that the nature of the dynamic inflow decay is better described by two rather than only one time constant. The dynamic changes in wake radius ~~were~~ are connected to the radial dependency of the axial induction transients. In conclusion, the comparative discussion of inductions, wake deployment and loads ~~facilitated the~~ facilitate an improved physical understanding of the dynamic inflow process for wind turbines. Furthermore, these measurements provide a new detailed validation case for dynamic inflow models and other types of simulations.

1 Introduction

Dynamic inflow describes the unsteady response of loads to fast changes in rotor loading, for example, due to fast pitching of the rotor blades or gusts. This unsteady aerodynamic effect leads to load overshoots due to the inertia of the global flow field, as the axial wake induction in the rotor plane cannot change instantaneously but only gradually to a new equilibrium flow field.

In addition to the direct impact on the dynamic loading, van Engelen and Hooft (2004) emphasise the need to model these dynamic inflow effects for the pitch controller design to enhance the stability and thus reduce unnecessary fatigue loads with optimised pitching transients, especially near rated operation. The dynamic wake behaviour due to load changes is intrinsically considered in higher fidelity approaches as Computational Fluid Dynamics (CFD) and Free Vortex Wake Method (FVWM)

1

simulations, thus modelling the dynamic inflow effect. However, engineering models are required to mimic this effect in Blade
Element Momentum (BEM) theory, which is commonly applied for aeroelastic simulations for the design and certification of
wind turbines. Well-tuned engineering models help to avoid too conservative predictions of fatigue loads.

First extensive studies in the 1990s within the Joule I and II projects on the development of dynamic inflow models for
wind turbines are described in Snel and Schepers (1995) and Schepers and Snel (1995). There the free field measurements of
out-of-plane blade root bending moment and rotor shaft torque for pitch steps on the 2 MW Tjæreborg wind turbine, described
in Øye (1991), are used for validation.

Later Schepers (2007) ~~employed~~ employ a one time constant model to analyse force transients. These ~~were~~ are derived from
pressure sensor arrays at five radial stations, after the pitch steps of the NREL phase VI turbine with 10 m diameter (see Hand
et al. (2001)) in the NASA Ames wind tunnel. Forces for the pitch step to low load ~~adapted~~ adapt faster to the new equilibrium
than for the step to high load. They could not experimentally validate the strong radial dependency of the time constant,
which they ~~expected~~ expect from cylindrical wake models. Sørensen and Madsen (2006) also ~~investigated~~ investigate the same
experiment and ~~compared~~ compare it to unsteady Reynolds Averaged Navier Stokes (uRANS) CFD simulations. They suggest
using a two time constant model to capture the dynamic inflow effect on the forces. The fast time constant represents the near
wake dynamics and decreases with radius and the slow time constant represents the far wake dynamics. Later Pirrung and
Madsen (2018) ~~investigated~~ investigate this experiment and uRANS CFD ~~simulation again and compared~~ simulations again
and compare them to a cylindrical wake model. Based on varying the wake length in the cylindrical wake model they affirm,
that two different time constants best describe the dynamic inflow effect.

In the MEXICO project, pitch steps ~~were~~ are performed on a 4.5 m diameter model wind turbine, featuring pressure distri-
bution measurements at five radial stations, as well as in high and mid-fidelity simulations (Boorsma et al. (2018)). They ~~found~~
find that unsteady aerodynamic effects on the blade chord level, namely the Theodorsen effect, reduce the load overshoot. This
effect can be modelled as a time lag on the angle of attack in the order of the ratio of relative wind to respective chord length.
In contrast, the typical dynamic inflow time constant is in the order of the ratio of radius to free wind velocity and two orders
of magnitude higher.

Yu et al. (2017) ~~used~~ use an actuator disk with variable blockage in a wind tunnel to study the wake evolution after a
change in thrust. We also ~~performed~~ present a preliminary pitch step experiment in see Berger and Kühn (2018), focusing on
the integral turbine loads~~(see Berger and Kühn (2018))~~. The relevance of improved modelling of the dynamic inflow effect can
be seen in the recent development of new dynamic inflow models by Yu et al. (2019), Madsen et al. (2020) and Ferreira et al.
(2021).

Schepers and Schreck (2018) emphasise on the value of experimental investigations of aerodynamic effects and also specif-
ically the dynamic inflow effect to further improve and validate models. Higher fidelity simulations depend on calibration and
thus cannot solely fill this gap. Further, Schepers and Schreck (2018) outline the importance of radius resolved aerodynamic
measurements over integrated blade and rotor loads. No experimental investigation is available until now, where the wake
induction is directly probed at various blade radii in the rotor plane.

The objective of this paper is to get deeper insights into the dynamic inflow effect for wind turbines due to pitch steps. The main novelty in this work is the dynamic induction measurement. ~~We investigated the~~ The radial dependency and differences between the pitch directions is investigated using time constant analysis. Furthermore, the behaviour of the flow in the near and close far wake and integral loads is used to compare the differences between the pitch directions. These different measurements are contemplated together to allow for new insights into the dynamic inflow effect, test presumptions and validate findings of prior works.

2 Methods

Here in Sect. 2.1 the experiment is introduced. In Sect. 2.2 time constant models and the fitting approach are outlined. Lastly, in Sect. 2.3 the method for the load reconstruction based on the obtained wake inductions is outlined.

2.1 Experiment

In this subsection, all relevant information on the experiment is introduced, consisting of the setup, experimental matrix, wake induction derivation from measurements, ensemble averaging approach, as well as correction models.

2.1.1 Setup

The experiments were performed in the large wind tunnel at ForWind - University of Oldenburg. It is a Göttingen type wind tunnel that can be operated in an open jet and a closed test section configuration. The test section length measures $30\,\mathrm{m}$ and the rectangular wind tunnel nozzle $3\,\mathrm{m}$ by $3\,\mathrm{m}$, as shown in Fig. 1 a. Wind velocities in the open jet configuration reach up to $32\,\mathrm{m\,s^{-1}}$. Kröger et al. (2018) provide detailed information about the wind tunnel and the optional active grid. No active grid was used in the measurement and the turbulence intensity of the inflow was in the order of $0.3\,\%$.
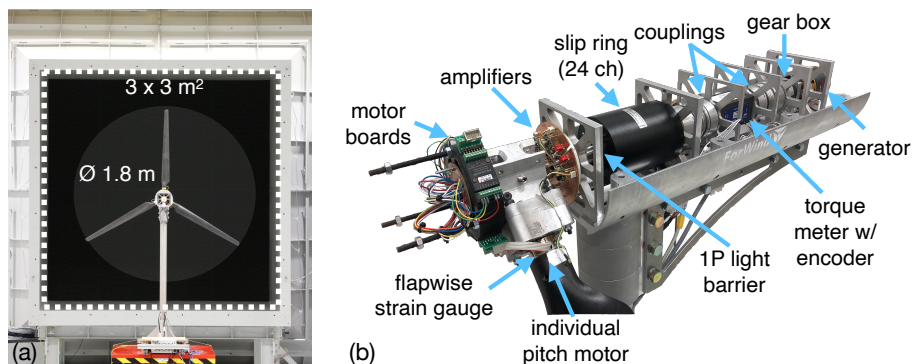

Figure 1. (a) Wind tunnel nozzle and MoWiTO 1.8 with main dimension. (b) MoWiTO 1.8 with open nacelle.

The utilised Model Wind Turbine Oldenburg has a diameter of $1.8\,\mathrm{m}$ (MoWiTO 1.8). The machine is an aerodynamically scaled version of the NREL 5 MW generic turbine (see Jonkman et al. (2009)) with a length scaling factor of $n_{length} = \frac{1}{70}$.

The scaling approach was to maintain the design tip speed ratio, thrust and power characteristic, as well as non-dimensional lift and thus axial induction distribution for the operational range. Low Reynolds number airfoils were used. The rotor blades have
80 a stiff carbon fibre-based structure with the first eigenfrequency of $32\,\mathrm{Hz}$ and estimated maximum tip deflections of $0.01\,\mathrm{m}$ The scaling approach and turbine are described in detail in Berger et al. (2018). The blockage ratio of the turbine in the used open jet configuration wind tunnel is 0.28, however, Ryi et al. (2015) showed that blockage effects are negligible for such an open jet configuration.

The MoWiTO 1.8 nacelle is shown in Fig 1 b. The turbine features individual pitch motors, which are mounted in the root
85 of each blade. The pitch motors are small DC motors with a three stage planetary gearbox with a gear ratio of 159:1 and integrated encoders. They are mounted pre-tensioned with springs to counteract gear backlashes and thus allow setting precise pitch angles. Pitching speeds up to ~~$100°\,\mathrm{s}^{-1}$~~ $100\,\mathrm{Hz}\,(1.75\,\mathrm{rad\,s}^{-1})$ can be achieved. The main shaft is supported by two roller bearings and connected by a coupling to a torque meter with an integrated encoder and through another coupling and one stage planetary gearbox to the generator. Flapwise blade root bending moments for each blade are measured by a full Wheatstone
90 bridge strain gauge configuration on the metal adapter, the carbon blades are glued on. The power supply for the amplifiers and motor boards in the hub and their communication with the control hardware is channelled through a slipring from the rotating hub to the stationary nacelle. Further, the thrust of the turbine is derived from a strain gauge measurement of the tower ~~foot~~ bottom bending in fore-aft direction, as outlined in Sect. 2.1.5. A National Instruments Compact Rio is used for control and data acquisition. Analog data (e.g. strain gauges, external hot wires) is sampled at 5 kHz and the control loop and pitch motor
95 communication run at 100 Hz.

The setup of the MoWiTO 1.8 in the wind tunnel is sketched in Fig. 2 a,b as a view from the side respectively top. The wind speed is obtained by the measured pressure drop in the wind tunnel nozzle. The turbine is positioned 2.6 diameter (D) behind the wind tunnel nozzle, so that the induction zone of the turbine is not influenced (see Medici et al. (2011)).

Integral loads of flapwise blade root bending moment (M_{flap}), rotor thrust (F_{thrust}) and rotor torque (M_{aero}) are obtained
100 based on strain gauge measurements shown in blue in the sketch.

Hot wire measurements in the near wake (up to $1\,D$ according to Vermeer et al. (2003)) and beginning far wake (more than $1\,D$) are performed at hub height. In flow direction (x-axis), seven distances ranging from $0.5\,D$ to $2\,D$ behind the turbine are considered in steps of $0.25\,D$ and shown in red in the sketch. In radial direction (negative y-axis), values between the rotor axis at 0 radii (R) to $1.4\,R$ in steps of $0.2\,R$ are considered. This adds up to 56 measurement positions.

105 In the rotor plane, Laser Doppler Anemometer (LDA) measurements are performed with a 2D system by TSI Inc.. A beam expander with a focus length of $2.1\,\mathrm{m}$ is used to not disturb the flow. Both lasers have a maximum power of $1\,\mathrm{W}$. The LDA probe is mounted on a three axes traverse system and can be motor-driven by $1.5\,\mathrm{m}$ in each direction. Measurement points are in the rotor plane at hub height. They are positioned radially (negative y-axis) from $0.25\,R$ to $0.95\,R$ with steps of $0.1\,R$ between $0.3\,R$ and $0.9\,R$ and the smaller extra steps at the edges of the range. The LDA measurement is indicated in green in
110 the sketch and the colour coding for the three signal types, strain gauge, hot wire and LDA, is maintained for all plots over time in this paper.

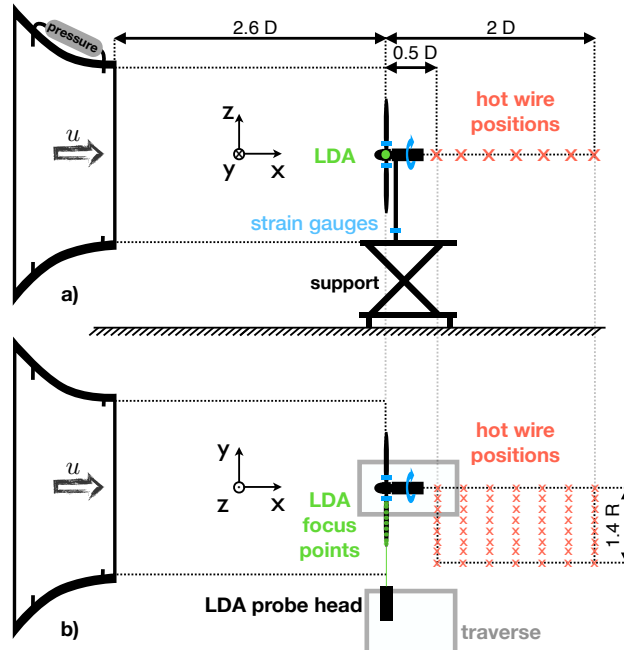**Figure 2.** Sketch of the setup in the wind tunnel. View from (a) the side and (b) the top.

2.1.2 Experimental matrix

The turbine is operated at a rotational speed of 480 rpm and wind velocity of $6.1\,\mathrm{ms}^{-1}$. This corresponds to a tip speed of $45\,\mathrm{ms}^{-1}$ and a tip speed ratio of 7.4. Chord based Reynolds numbers range from a minimum value of $60 \cdot 10^3$ at the first airfoil
115   at $0.2\,R$ to values between $100 \cdot 10^3$ and $120 \cdot 10^3$ from $0.5\,R$ to the tip. Time constants in dynamic inflow models are related to a reference time constant $\tau_{ref} = R/u_0$ (see Schepers (2012)). This amounts to $0.15\,\mathrm{s}$ here.

The rotor blades are collectively pitched by $5.9°$ between $-0.9°$ and $5.0°$, within $0.070\,\mathrm{s}$, corresponding to about half a rotor revolution and half the reference time. The pitch step is from a low rotor load at a thrust coefficient $C_T = 0.48$ to a high load at $C_T = 0.90$ and vice versa, based on the strain gauge derived thrust. This corresponds to rotor effective inductions of
120    $a_{eff} = 0.14$, respectively $a_{eff} = 0.34$, based on the momentum theory relation ($C_T = 4a(1-a)$).

The representative encoder reading of one pitch motor is plotted in Fig. 3. Between the pitch steps, there are $3\,\mathrm{s}$ (24 revolutions) to allow for the flow to reach an equilibrium again. There is a slight overshoot of the pitch angle for both pitch directions by one encoder step ($0.18°$), which due to the small value has no noticeable effect on our investigation.

For the LDA measurements, 100 pitch steps were performed for each radial position and pitch direction at a typical sampling
125   frequency of $600\,\mathrm{Hz}$. This sampling frequency is just an order of magnitude since it depends on many parameters, especially the seeding of tiny oil droplets in the wind tunnel and thus varies constantly. Load measurements are taken during the LDA measurements. Therefore load signals for 900 pitch steps are available. The hot wire measurements have been performed separately. A wake rake consisting of four hot wires was used to measure at the described 56 positions in the wake. Thus the
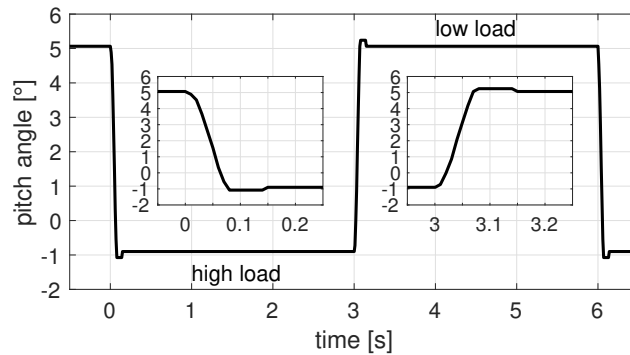
5

Figure 3. Pitch motor encoder signal for a pitch step to high load followed by a step to low load with additional zoomed in views of the actual pitch steps.

experiment, consisting of 25 pitch steps, had to be performed $56/4 = 14$ times and the wake rake was moved between those measurements.

2.1.3 Wake induction measurement by 2D-LDA

The wake induction is derived from the LDA measurements by a method introduced by Herráez et al. (2018) for steady operation. The method uses the local velocity in the rotor plane, free of the influence of the bound circulation. This velocity is obtained by probing in the bisectrix of two rotor blades for axial and uniform inflow. In the bisectrix, the ~~blade~~ blades induction is counterbalanced and thus cancelled out. This method ~~is less suited for the root and tip region of the blade, as the effect of trailed vorticity is not caught.~~

In Fig. 4 a the MoWiTO turbine is shown with the LDA laser beams and the probed axial (u_{ax}) and tangential (u_{ta}) velocity components at a specific radius. Alongside in Fig. 4 b, the concept of the counterbalancing of the bound circulation of the evenly loaded blades is sketched. ~~The tower~~ For the shown position the blade at the 9'o clock position has no influence on the axial velocity on the indicated line of measurements. At that line the downwash of the blade ahead of the indicated line counteracts the upwash of the blade behind it and they cancel each other. The velocity at the line thus is only influenced by the wake induction. Herráez et al. (2018) argue, that the trailed vorticity especially at the tip might play a non-negligible role, as it cannot be captured well at the high distance between the measurement position and the blade tip. Therefore the method is less suited for the root and tip region of the blade.

Two constraints defined the line of LDA measurements. The first is the height range of the LDA probe head, which is from tower bottom to hub height. The second is to minimize the influence of the tower on the blade nearest to the tower for the measurements in the bisectrix of two blades. This led to a measurement line at the 3'o clock position. The tower does disturb the axial symmetry, however, based on an estimation of the tower effect with a dipole model as in Schepers (2012) the tower effect ~~at the measurement positions~~ on the 5'o clock blade position is considered negligible.
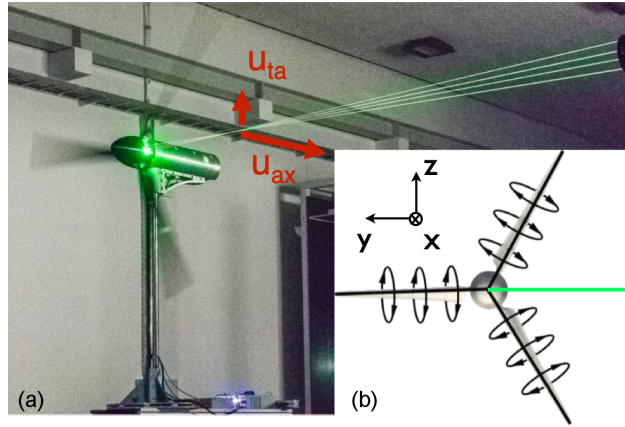
Figure 4. (a) ~~Rotating~~ Clockwise rotating MoWiTO 1.8 with 2D-LDA probing axial u_{ax} (along x-axis) and tangential u_{ta} (along z-axis) velocity components in the bisectrix of two blades. (b) Scheme of ~~principle of~~ counterbalancing bound circulation of the evenly loaded blades ~~in the bisectrix,~~ of front view of clockwise rotating rotor. The LDA measurement line is indicated in ~~red~~ green (adapted from Herráez et al. (2018)).

To obtain the values in the bisectrix, ~~we synchronised~~ the LDA system is synchronised with the MoWiTO data acquisition system. Measurements at ~~constant~~ the constant high load are plotted for one position of the axial and tangential probe over the azimuth angle ϕ_1 of the turbine in Fig. 5. The bisectrix values that are in a threshold of $\pm 3°$ are marked in red. ~~We identified these threshold values~~ These threshold values were identified to give a good compromise between data points and data quality. ~~Note that the axial probe does look like the theoretical derivation of the signal in reference Herráez et al. (2018)~~ In Fig. 5 a also the analytical course seen by the axial probe according to Herráez et al. (2018) (see App. A), is presented and shows a good match to the measured signal. This good fit gives a high level of confidence on the applicability of the method to this experiment. For the tangential probe, data is missing around $-1.3\,\mathrm{m\,s^{-1}}$ and also at $2.3\,\mathrm{m\,s^{-1}}$ for the axial probe, which is due to the beta status of the LDA system at that point in time. We were aware of this bug and it has no influence on the presented measurements.

Based on these measured axial and tangential velocities, the undisturbed inflow velocity u_0 and the angular velocity Ω, the axial (a) and tangential (a') wake induction factors are defined by Eq. (1) and Eq. (2). With the geometrical angle ~~of the rotor segment (θ)~~ γ between the chord of the local blade segment and the rotor plane, consisting of twist and pitch, the angle of attack α can be calculated by Eq. (3).

$$a = 1 - \frac{u_{ax}}{u_0} \tag{1}$$

$$a' = \frac{u_{ta}}{\Omega r} \tag{2}$$

$$\alpha = \arctan\left(\frac{u_{ax}}{u_{tan} + \Omega r}\right) - \underset{\sim}{\theta}\,\gamma \tag{3}$$
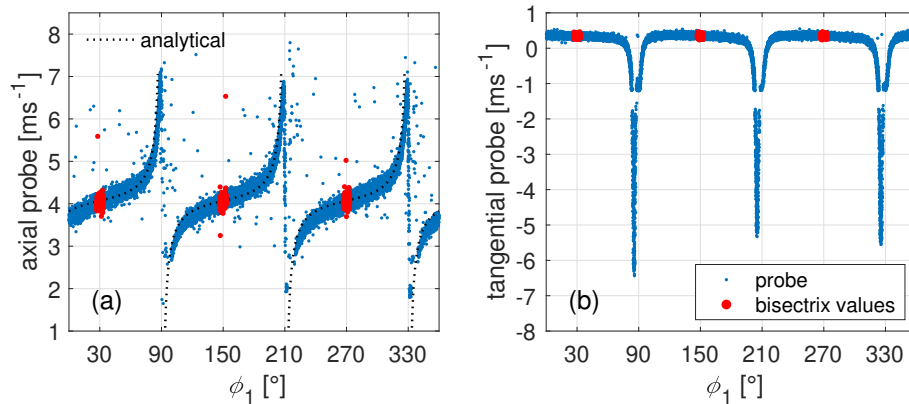
Figure 5. (a) Measurements of axial probe for high load case at a radius of $0.7\,R$ for 400 revolutions over azimuth angle ϕ_1 with marked data within the bisectrix threshold. $\phi_1 = 0^\circ$ relates to the 12 o'clock position of blade 1. (b) Analogously for the tangential probe.

The method was validated based on particle image velocimetry (PIV) measurements and CFD calculations of the MEXICO rotor by Herráez et al. (2018) for steady operation. They found a good performance of the method from $0.3\,R$ up to $0.9\,R$. In Rahimi et al. (2018), the model was further compared to alternative approaches applied to CFD simulations. Based on these
170   comparisons and ~~our~~ the specific focus on the dynamic change of inductions, rather than the total values, ~~we considered~~ the agreement at the root radius at $0.25\,R$ and the tip radius at $0.95\,R$ is considered still reasonably good. Therefore ~~we~~ it is decided to include these radii in this analysis. However, they should be treated with care.

2.1.4   Ensemble averaging

Ensemble averages are used for the LDA data, hot wire and strain gauge measurements. The data of many repetitions is aligned,
175   triggered by the pitch command. An average value at each time step is constructed out of this data, for the time span $-0.5\,\mathrm{s}$ to $3\,\mathrm{s}$, with the pitch step starting at $0\,\mathrm{s}$. For example, the ensemble average of the flapwise blade root bending moment M_{flap} is given by Eq. (4), with the counter of cycles n, total cycles N and the time t.

$$M_{flap}(t) = \frac{1}{N} \sum_{n=1}^{N} M_{\mathrm{flap,\ single\ cycle}}^{(n)}(t) \tag{4}$$

This approach can smooth out non-deterministic variations and also structural interactions. In Fig. 6 a, the flapwise blade root
180   bending moment for the step to low load is shown for single cycles and the ensemble average. As the pitch step is not aligned with the rotor position, the effect of the tower shadow, seen for the single cycles, is smoothed out for the ensemble average. The high number of 900 repetitions, due to the nine different LDA positions with 100 pitch steps each, leads to a very small 95% confidence interval (CI), which would barely be visible in the plots and, therefore, is not shown here or later load-related plots.
185   The induction factors have no fixed sampling frequency, as firstly, the underlying LDA measurements are non-equidistant and secondly, only values within the bisectrix of two blades are considered. To construct a single ensemble average out of

this data, ~~we sort~~ the 100 repetitions per LDA position are sorted to one signal and ~~use~~ a smoothing approach based on local regression and a weighted least squares and first order polynomial model is used. For the local regression, 1% of the data (length of the total dataset is $4.5\,\mathrm{s}$) is used, whereas outliers get weight penalties and are not considered for more than six standard deviations. This filter is implemented as 'rlowess' within MatLab 2019b. This smoothed ensembled LDA based data is resampled to $1\,\mathrm{kHz}$, reducing the original non-equidistant data points by a factor of about 3. The sorted data points along the smoothed resampled signal and 95% CI for the axial rotor plane (rp) velocity at $0.7\,R$ for the step to low load are shown in Fig. 6 b.
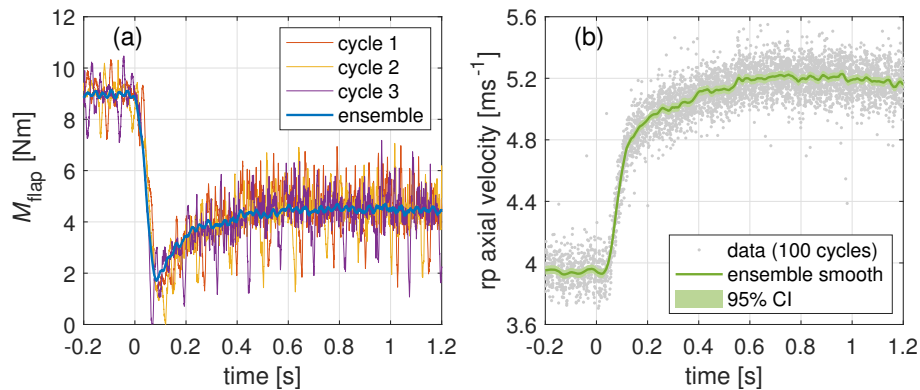

Figure 6. (a) Single cycles and ensemble average of flapwise blade root bending moment M_{flap}. (b) Data points and smoothed ensemble average for axial rotor plane (rp) velocity in bisectrix of blades.

2.1.5 Corrections

~~We applied steady corrections~~ Steady corrections are applied to the thrust and torque signals. For the torque, the mechanical torque is measured at the torque meter. To obtain the aerodynamic rotor torque, ~~we calibrated~~ the friction in the bearings and the slip ring was calibrated by running the drivetrain without blades with the motor, used as a generator in operation, and thus ~~measured the friction~~ the friction was measured with the torque meter. ~~We obtained a~~ A linear function of the angular rotor speed ~~and added~~ was obtained and the respective value added to the signal.

The rotor thrust is derived from the tower ~~foot~~ bottom bending moment in fore-aft direction. The strain gauge was calibrated using defined forces in the thrust direction applied to the nacelle at the height of the rotor axis. The tower and nacelle drag was experimentally calibrated with the turbine without blades and was subtracted from the signal. ~~We used the~~ The free stream velocity (u_0) was used for this correction rather than a corrected wind velocity. This does lead to a small underprediction of the thrust. This error, however is smaller as if ~~we did not do a correction at all~~ no correction would be applied. In contrast to a dynamically corrected rotor plane wind velocity, this correction is a fixed value that does not influence the main shape of the dynamic load transient.

Dynamic corrections were considered for the torque and thrust signal. Directly after the pitch step, the torque control cannot keep the rotor speed completely steady, so there was a minor deviation of a maximum of 2% of the rotor speed. ~~We used~~ Eq. (5) is used to correct the torque by the contribution ΔM associated to the angular acceleration $\dot{\Omega}$, where I_{rot} is the equivalent rotational inertia of the rotor and drivetrain.

$$\Delta M(t) = I_{rot} \cdot \dot{\Omega}(t) \tag{5}$$

After the pitch step, there is an oscillation of the tower, which is seen in the tower ~~foot~~ bottom bending moment. ~~We estimate the~~ The eigenfrequency of the tower and the damping constant of the oscillation is estimated iteratively and thus ~~correct~~ the measurement signal is corrected to obtain the aerodynamic thrust. The signals without the dynamic correction will also be shown in the results section as a reference (see Fig. 19).

2.2 Time constant analysis

The decay process after the pitch step is investigated in terms of time constant analysis. Firstly, a one component time constant model (1c), like used by Schepers and Snel (1995) is applied, given by Eq. (6) for the arbitrary signal S.

$$S(t) = S_{t_0} - \Delta S \cdot \left(1 - \exp\left(\frac{(t_0 - t)}{\tau_{single}}\right)\right) \tag{6}$$

In Fig. 7 a, the fitting approach is outlined for an exponential transition to a higher value without an overshoot, representing the behaviour that is expected from an induction transient. Figure 7 b shows a signal with an overshoot and subsequent exponential decay to the new steady level. This represents the behaviour expected from a load. The fit starts when the pitch step is terminated at $t_0 = 0.070\,\text{s}$ at the signal value S_{t_0}. The new steady level after the pitch step is S_1, being the mean value from $t = 2\,\text{s}$ to $t = 3\,\text{s}$. The difference ΔS is given by $S_{t_0} - S_1$ and also contains the information on the direction. The time constant τ_{single} is fitted by means of the least root mean square error for the fitting range between $t_0 = 0.070\,\text{s}$ and $t_{\text{fit}} = 0.80\,\text{s}$.
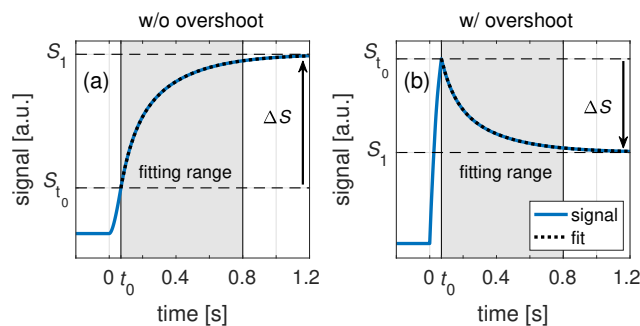

Figure 7. (a) Time constant fitting scheme for a signal with exponential decay behaviour without an overshoot. (b) Analogously for a signal with an overshoot.

Secondly, ~~we use~~ a model with two time constants (2c) ~~,~~ similar to Sørensen and Madsen (2006) is used. The fitting model is given by Eq. (7). The fitting procedure is according to the single time constant model. However, three values are fitted, a fast

time constant τ_{fast}, a slow time constant τ_{slow} and the weighting factor k of each exponential decay function, associated with the two time constants.

230 $$S(t) = S_{t_0} - \Delta S \cdot \left((1-k) \cdot \left(1 - \exp \frac{(t_0 - t)}{\tau_{fast}} \right) + k \cdot \left(1 - \exp \frac{(t_0 - t)}{\tau_{slow}} \right) \right) \tag{7}$$

These time constants can be used for comparison and tuning of the time constants in the dynamic inflow engineering models of Øye (see Snel and Schepers (1995)), used in OpenFAST and GH Bladed, and the new DTU model (see Madsen et al. (2020)), used in HAWC2. The time constants of these engineering models are derived from simulations and parametrised to the turbine size and operational condition considering the relevant dynamic inflow time scaling factor $\frac{u_0}{R}$, the radial position and

235 the quasi-steady axial induction factor.

2.3 Load reconstruction from induction measurement

Additionally to the strain gauge measured integral turbine loads, these loads are also reconstructed based on the induction measurements. The angle of attack along the rotor blade are already derived from the experiment through Eq. (3). The relative velocity ~~v_{rel}~~ u_{rel} is given by Eq. (8). Hence, the information obtained by the momentum part of a BEM code is known from

240 the experiment. So ~~we use~~ the blade element theory (BET) part of a standard BEM code as outlined in detail by Hansen (2008) is used. The force for the blade segments can be calculated for the normal direction according to Eq. (11) and for the tangential direction according to (12), where the lift force of the segment is given by Eq. (9) and the drag force by Eq. (10). The inflow angle is defined by θ.

$$\underline{v}u_{rel} = \sqrt{u_{ax}^2 + (u_{ta} + \Omega r)^2} \tag{8}$$

245 $$F_L = \frac{1}{2} \cdot C_L(\alpha) \cdot \rho \cdot \Delta r \cdot c \cdot \underline{v}u_{rel}^2 \cdot F \tag{9}$$

$$F_D = \frac{1}{2} \cdot C_D(\alpha) \cdot \rho \cdot \Delta r \cdot c \cdot \underline{v}u_{rel}^2 \cdot F \tag{10}$$

$$F_N = F_L \cos\theta + F_D \sin\theta \tag{11}$$

$$F_T = F_L \sin\theta - F_D \cos\theta \tag{12}$$

$C_L(\alpha)$ and $C_D(\alpha)$ are the lift and drag coefficients for the respective angle of attack. These lift and drag polars are obtained

250 by XFoil (see Drela (1989)). The ~~blade~~ lift polars are corrected for 3D effects, as lift coefficients on rotating blades can be significantly higher than for a stationary blade due to the effect of cross lows related to a stall delay. This effect is most relevant for the root airfoils and was corrected by the method by Snel et al. (1993). The blade segment width is Δr and c the chord length. The air density is given by ρ. The factor F accounts for the tip losses based on the Shen et al. (2005) tip loss model. The integral load signals are reconstructed by integration of the forces along the rotor blade.

255 The influence of unsteady airfoil aerodynamics (uA) on the blade level, namely the Theodorsen effect, is not contained in the axial wake induction and therefore has to be additionally considered in the reconstruction. ~~We used the~~ The implementation

11

given in detail in Pirrung et al. (2017) is used. This is the inviscid part of the unsteady aerodynamics model by Hansen et al. (2004), which treats the shed vorticity effects due to fast angle of attack changes as a time lag on the angle of attack α and has been extended to take the effect of camber into account. Thus, the magnitude and direction of the aerodynamic forces are

260   influenced. The ~~typical time lag of this~~ main model is reproduced in App. B. The typical uA time constant which determines the lag of the angle of attack due to the uA effect is in the order of ~~c/v_{rel}~~ $\frac{c}{u_{rel}}$, whereas the typical time constant of the dynamic inflow effect is ~~R/u_0~~ $\frac{u_0}{R}$ and at least two magnitudes of size larger, as mentioned in Sect. 1. Reconstructed loads will be investigated with and without the uA model.

3   Results

265   Here the measurement results are described. In Sect. 3.1 the induction in the rotor plane is shown as a function of radial position determined ~~along the procedure from~~ with the procedure described in Sect. 2.1.3. Then Sect. 3.2 shows the wake measurements from the hot wires as a function of streamwise position at hub height. Finally Sect. 3.3 presents the loads as measured from the straing gauges and the loads derived from the induction measurements according to the procedure of Sect. 2.3.

3.1   Induction results

270   In Fig. 8 a, the measured axial inductions, in Fig. 8 b, the tangential inductions and in Fig. 8 c, the derived angle of attack from the LDA measurements are presented for the steady high and low load cases. For the high load case, the axial induction
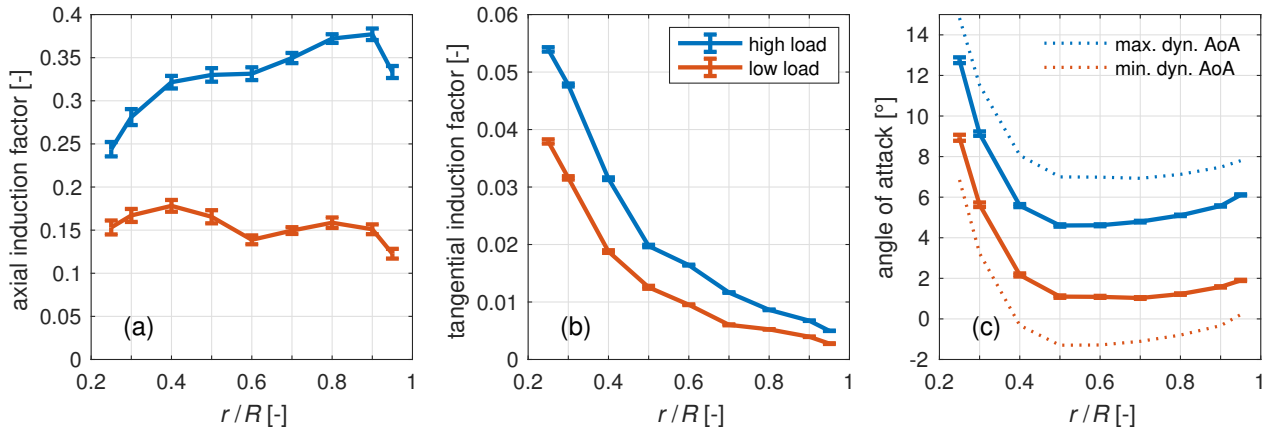

Figure 8. (a) Axial and (b) tangential wake induction factors and (c) derived angle of attack distribution from the LDA measurements for the steady high and low load case. The errorbars denote the 95% confidence interval, based on the measured data for axial and tangential velocity in the rotor plane considering 100 measurement cycles.

has values between 0.25 near the root ($0.25\,R$) and 0.38 near the tip ($0.9\,R$), in general with an increasing trend with radius apart from the tip nearest radius. The low loaded case has a more uniform loading with values between 0.12 and 0.18. For

comparison, the rotor equivalent axial induction obtained from momentum theory ($C_T = 4a(a-1)$) with C_T based on the strain gauge measurements do give similar values of 0.34, respectively 0.14.

The tangential induction for both cases is high near the root and decreases with radius with a high rate in the beginning and then more gentle. Due to the larger rotor torque, the high load case shows higher values.

The angle of attack distribution for the high load and low load case shows angles of attack of $4°$ to $6°$ for the high load case from $0.4\,R$ on and $1°$ to $2°$ for the low load case. The values increase towards the root for both cases. The stall angle is estimated as the angle of attack with the highest lift coefficient, where the flow is not completely separated. This angle for the used airfoils at the respective Reynolds number of the experiment is at $15°$ for the root airfoil used up to $0.4\,R$ and at $11.5°$ for the tip airfoil used from $0.5\,R$ on. Thus, the considered range of the blade is operating outside of the stall regime for both load levels for the steady states.

The observed difference between the two angle of attack distributions is smaller than the pitch step value of $5.9°$ the blades do pitch. This is due to the flow through the rotor and induction factors that change between the two steady operational states. From this information the maximum angle of attack range can be estimated a priori, in order to assess the flow conditions during the pitch steps. The dynamic maximum and minimum angle of attack distributions are estimated for an infinitely fast pitch step. We assume in a mind experiment that the flow field of the steady state before the pitch step is unchanged, but the pitch step and thus geometrical change of the inflow angle is already done. This allows to estimate the extreme dynamic angles of attack, neglecting any damping uA effects for the infinitely fast pitch step.

These maximum and minimum dynamic angles of attack are shown in dotted lines in Fig. 8 c. For the step to high load the stall limit is approached at nearly $15°$ angle of attack at the root near radius of $0.25\,R$. For the step to low load, there is a minimum dynamic angle of attack of about $-1.5°$ in the middle of the rotor blade. This lowest angle of attack gives a lift coefficient of zero. For a finitely fast pitch step the flow already adapts during the pitch step and the extreme dynamic values are closer to the new steady values. The uA effects further damp the overshoot of angles of attack. So apart from the blade root at the step to high load, where the stall limit is approached, the blade is operated outside the stall region for the pitch steps.

The axial induction factor transients are shown in Fig. 9 for four different radii ($0.3\,R$, $0.5\,R$, $0.7\,R$ and $0.9\,R$) for both pitch steps. They show direct evidence of dynamic inflow where the induction factors and therefore induced velocities reach the new equilibrium value only slowly.

The fits of the one (1c) and two time constant (2c) models are also shown in the plots. The fits start from the instance the pitch step is terminated at t_0. At that time the axial induction has already adapted by about $28\,\%$ on average of the difference between the steady axial induction levels for the radii from $0.3\,R$ to $0.9\,R$ independent of the pitch direction.

The fitted time constant τ_{single} of the 1c model is plotted over the radius for both pitch directions in Fig. 10. In the root near region up to $0.4\,R$ both pitch directions show similar values apart from the radius at $0.25\,R$, where the step to high load has a higher time constant. For radii from $0.5\,R$ on the step to high load shows higher values than the step to low load. There is no
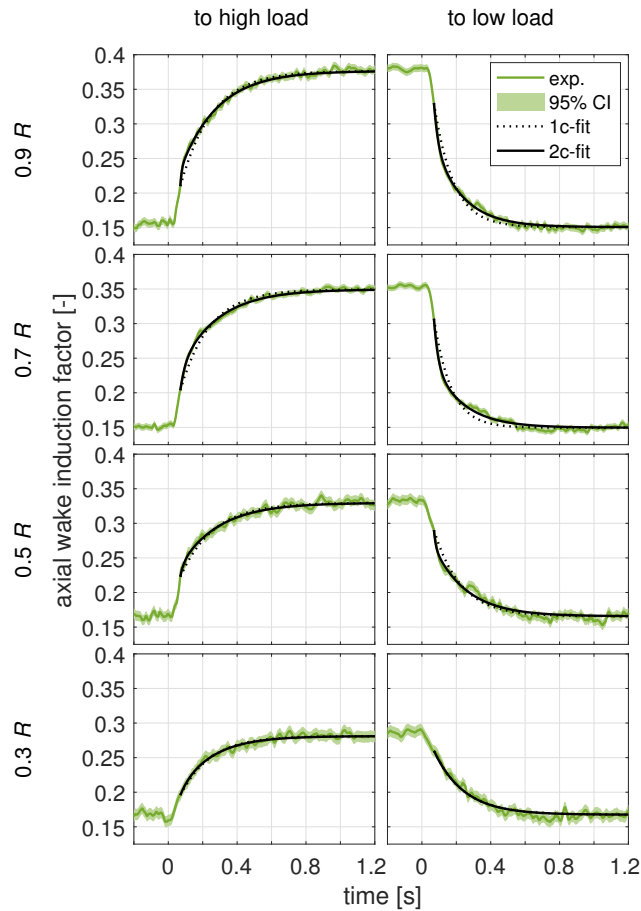
Figure 9. Axial wake induction factor over time for pitch step to high load and low load for the four radii $0.3\,R$, $0.5\,R$, $0.7\,R$ and $0.9\,R$ and the fitted exponential decay models with one time constant (1c) and two time constants (2c).

clear trend obvious for the step to high load. In contrast, for the step to low load, there is a trend towards reduced time constants towards higher radii.

310   In Fig. 11, the three fitting parameters of the 2c model are presented. In the top row, the three fitted variables $k = k_{\text{free}}$, τ_{fast} and τ_{slow} are plotted over the radius. Near the root at $0.25\,R$ the k value for both pitch directions has a value of 1 respectively nearly 1, indicating no contribution from τ_{fast}, which consequently is also not plotted for these radii. For radii up to $0.5\,R$ the values for the step to low load have a higher k_{free} value than for the step to high load, switching from $0.6\,R$ on to the tip. τ_{fast} does have similar values from $0.4\,R$ to the tip and for both pitch directions. ~~Values towards the root are higher, however,~~

315 ~~the root nearest value is not relevant for the fit, as there k_{free} equals 1. Thus, the~~ Towards the root the decay process is only defined by τ_{slow} there, as k_{free} equals or nearly equals 1. For τ_{slow} there is no clear radial trend for both pitch directions, but a clear difference between pitch directions. For the step to high load τ_{slow} is higher for all radii than for the step to low load.
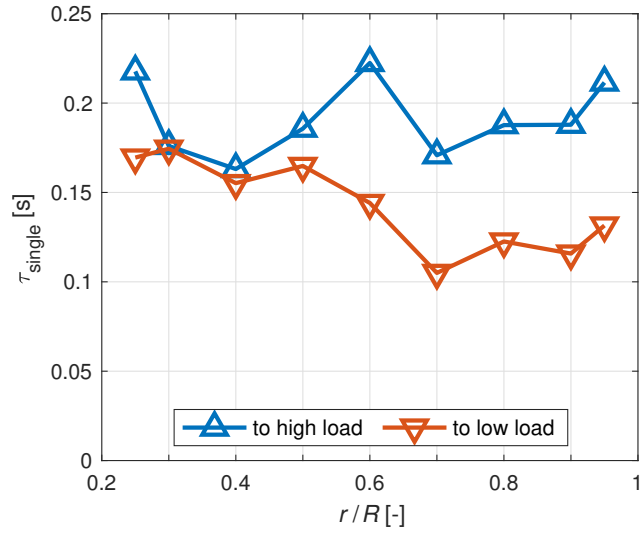
14

Figure 10. One time constant model fit of τ_{single} to the axial wake induction factor over the radius for both pitch directions.
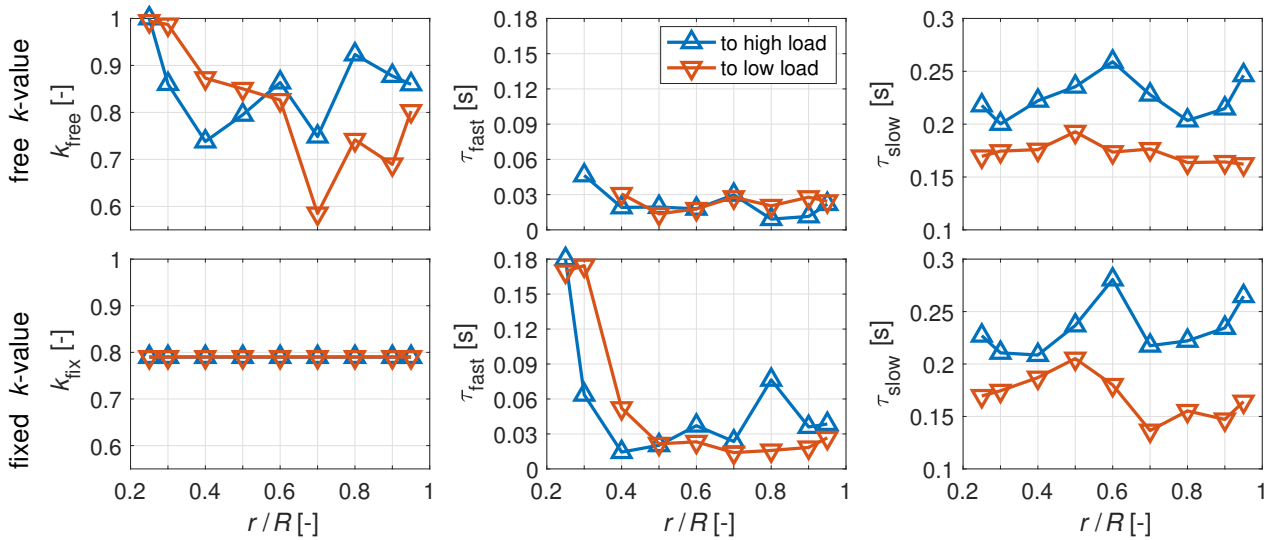

Figure 11. Two time constant model fit to the axial wake induction factor, derived from the rotor plane LDA measurements with the ratio k and the fast τ_{fast} and slow τ_{slow} time constants. In the top row the k value is fitted as a free parameter. In the bottom row the weighting ratio of fast and slow time constant k is fixed (to the mean value of both pitch directions and radii of the fit in the top row).

15

Due to the ~~influnece~~ influence of the varying weighting ratio of fast and slow time constant, a direct comparison of these time constants is limited.

To overcome this limitation, the ratio k is fixed to a value of $k_{\text{fix}} = 0.79$, which is the mean value for all radii of both pitch directions of k_{free}. With this setting τ_{fast} contributes by 21% to the decay of the axial induction. This fit is shown in the bottom row of Fig. 11.

The fitted τ_{fast} is high near the root for both pitch directions. For the step to high load τ_{fast} decreases from the root to $0.4\,R$, after which there is ~~a slight~~ an increase again (ignoring an outlier at $0.8\,R$). From $0.5\,R$ to $0.9\,R$ τ_{fast} increases by 67%. For the step to low load τ_{fast} has ~~nearly~~ more constant values from $0.5\,R$ to $0.9\,R$, decreasing by 14%. Hence τ_{fast} is ~~shorter~~ smaller for the negative load step, for radii larger than $0.5\,R$, which represents 75% of the rotor swept area.

Values of τ_{slow} are slightly higher for the step to high load and show more variation than in the prior fit with $k = k_{\text{free}}$ ratio. There is a slight radial trend to higher values, with an increase in τ_{slow} from $0.3\,R$ to $0.9\,R$ by 11%. For the step to low load also more variation is apparent and a slight radial trend towards lower values is indicated, with a decrease in τ_{slow} from $0.3\,R$ to $0.9\,R$ by 16%. Taking the mean value over radius, the slow time constant for the step to low load is about 28% lower.

The fitting accuracy of the applied models is determined based on the root mean square error (RMSE) in the fitting range t_0 to t_{fit} between the measured signal and the respective fitted model and plotted over the radius in Fig. 12. For both step

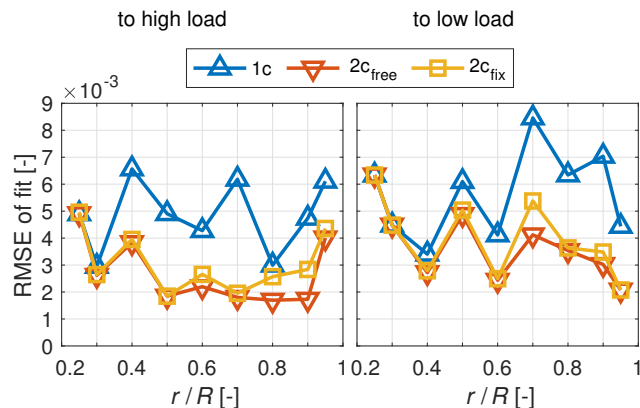**Figure 12.** Root mean square error (RMSE) between measured axial wake induction factor and the three fitted models, 1c-fit and 2c-fit with k_{free} and k_{fix} for both pitch directions.

directions, there is no difference in RMSE for the root near stations up to $0.3\,R$ between the fitting models, which are the 1c and 2c model, once with $k = k_{\text{free}}$ and once with $k = k_{\text{fix}}$. For higher radii the error of the 1c fit is higher than for the two variants of the 2c model. The differences between the two variants of the 2c model are small, showing that there is only a small penalty for fixing the k ratio .

The tangential wake induction factors over time for both pitch directions are presented for the four radii $0.3\,R$, $0.5\,R$, $0.7\,R$ and $0.9\,R$ with the fit of the 1c model in Fig. 13. In contrast to the axial induction, the tangential induction shows an overshooting behaviour. The exponential fit starts around t_0 at the respective minimum or maximum peak, as this showed to
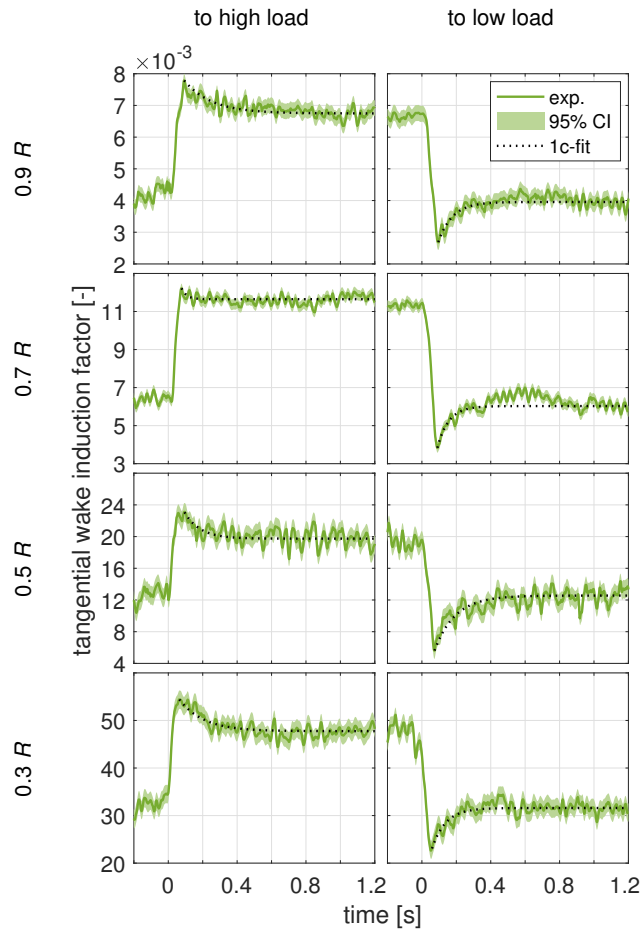
16

Figure 13. Tangential wake induction factor over time for pitch step to high load and low load for the four radii $0.3\,R$, $0.5\,R$, $0.7\,R$ and $0.9\,R$ and the fitted exponential decay model with 1 time constant (1c).

340 improve the fitting. The starting point of the fit thus varies between $0.059\,\mathrm{s}$ and $0.095\,\mathrm{s}$, with a mean value of $0.074\,\mathrm{s}$. The overshoot, in general, seems more prominent for the step to low load and only barely present within the signal noise at the radius of $0.7\,R$ for the step to high load.

The fitted τ_{single} values to the 1c model are plotted over radius for both pitch directions in Fig. 14. Cases where the overshoot is smaller than three standard deviations of the filtered signal of the new equilibrium were excluded due to a very high sensitivity

345 on the starting point of the fit.

For the step to high load, only two radii at the root and two radii near the tip fulfil this requirement, whereas for the step to low load only the tip most radius at $0.95\,R$ is excluded. For the radii where values for both pitch directions are available, the step to high load shows higher τ_{single} values. For both pitch directions, τ_{single} is lower than the corresponding τ_{single} for the
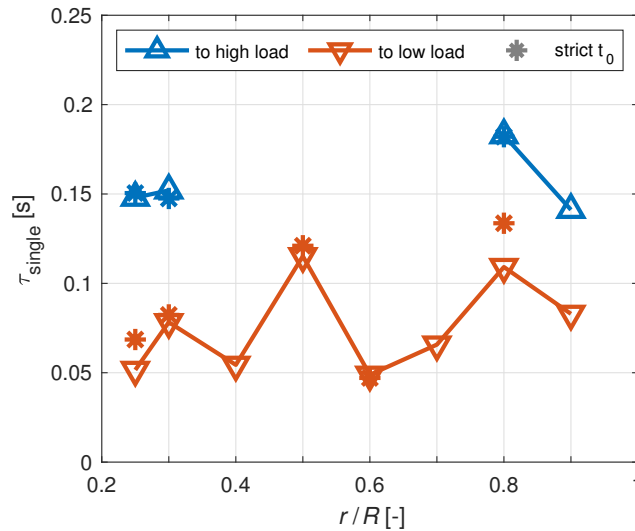
Figure 14. One time constant model fit of τ_{single} to the tangential wake induction over the radius for both pitch directions.

axial inductions. We ~~do~~ see no connection of this unexpected overshooting behaviour of the tangential induction to the slight
350   rotor speed deviations, which are present between $0\,\text{s}$ and $0.6\,\text{s}$ and thus at a time frame up to one magnitude of order higher.

The influence of the small allowed shift in the start of the fit is also investigated. For a strict starting point of the fit at t_0, shown in Fig. 14 as stars, the set criterion of overshoot to noise is fulfilled for only three radii for the step to high load and five radii for the step to low load. For the available radii however there are only negligible differences to the shown fit in comparison to the observed spread.

355   **3.2 Wake results**

In the following the hub height hotwire measurements downstream of the turbine in the near and close far wake up to $2D$ downstream are analysed. The wake measurements are shown as a surface plot for four different timestamps in Fig. 15, for both pitch directions and normalised by the free stream velocity. The first contours at $t = 0\,\text{s}$ are the starting equilibrium condition. For the step to high load, the initial wake, being the steady low load case, shows wake velocities around $0.8\,u_0$
360   coloured in green tones for $0.2\,R$ to $1\,R$ radial positions. For the step to low load, the initial velocity field in the wake, being the steady high load case, is around $0.5\,u_0$, cloured in blue tones. The dotted red line is the isoline of $0.9\,u_0$, which ~~we use~~ is used as an indication of the wake streamtube.

The contours for the following time stamps show the transition to the new steady state. These transitions seem at first glance different for the two pitch directions. For both pitch directions at $t = 0.4\,\text{s}$ and at around $1\,D$ to $1.25\,D$ there seems to be the
365   transition line where old and new wake meet. The indicated wake radius shows, that the dynamic wake streamtube is constricted at $1\,D$ for the step to high load, whereas it is widened up for the step to low load. This behaviour is opposite to what ~~we do expect~~ is expected for the new steady streamtubes, where for the step to high load, the wake widens, due to the higher thrust.

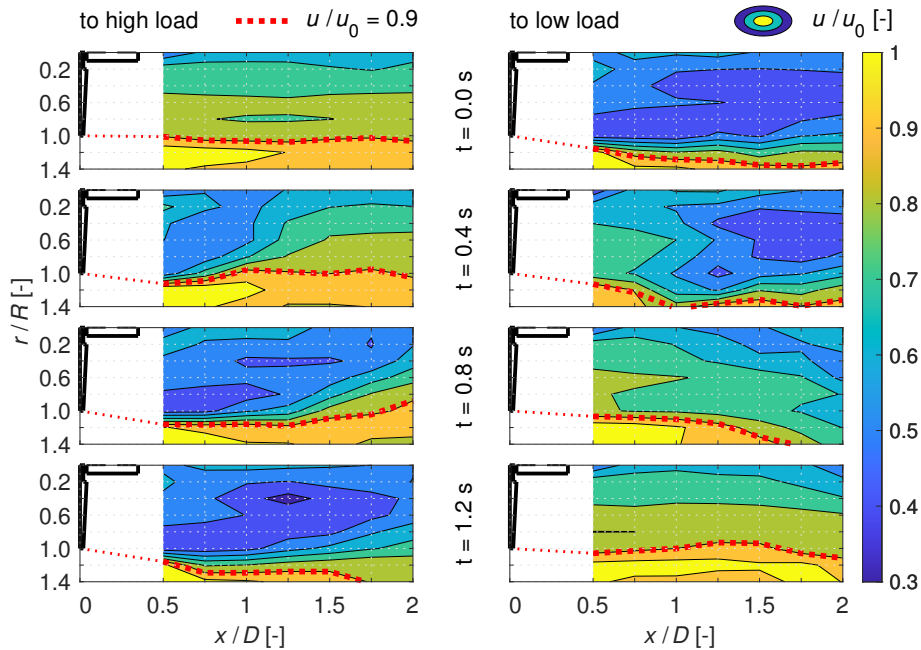**Figure 15.** ~~Velocity~~ Top view on velocity contour in the horizontal plane at hub height of the wake at the four different time stamps, $0\,\mathrm{s}$, $0.4\,\mathrm{s}$, $0.8\,\mathrm{s}$ and $1.2\,\mathrm{s}$ after the pitch steps to high and to low load, normalised by the free stream velocity. The turbine dimensions are indicated in correct scale in the plots as a reference, with the x-axis being the axis of rotation.

Further, it narrows due to the lower thrust for the step to low load. For the time stamp at $t = 0.8\,\mathrm{s}$ a similar picture can be seen where this transition between old and new wake has progressed to around $1.75\,D$. The figure at the left bottom is very similar to the figure at the right top and the same holds for the figure at the right bottom and left top. This indicates that the new equilibrium is approached at $t = 1.2\,\mathrm{s}$.

To further interpret this measurement, normalised velocity contours are presented as the difference to the new equilibrium steady state in Fig. 16. The normalised difference is defined as $\Delta u/u_0$, with $\Delta u = u_t - u_\infty$, where u_t is the velocity at the respective time at a measurement position and u_∞ the velocity at the same point at the new steady condition after the pitch step. Therefore, a value of 0.5 means that the wake has to adapt by $0.5\,u_0$ to reach the new equilibrium. The starting conditions for both pitch directions look alike, as they show the difference between the two steady states. At the timestamp of $t = 0.4\,\mathrm{s}$ ~~we see~~ a very similar shape of this potential like area is seen for both pitch directions. A widening of the wake for the step to low load is indicated when concentrating on the orange field near the tip radius, which is at a radial position of $1\,R$ for the step to high load and at $1.2\,R$ for the step to low load. For the step to low load, this orange maximum has travelled further than for the step to high load. At the timestamp at $t = 0.8\,\mathrm{s}$ the wake for the step to low load has ~~adopted~~ adapted more to the new steady state than for the step to high load. At the timestamp of $t = 1.2\,\mathrm{s}$ for the step to low load, the equilibrium is reached. For the step to high load, the wake has not completely adapted to the new equilibrium with still a clear lighter blue area at $2\,D$.
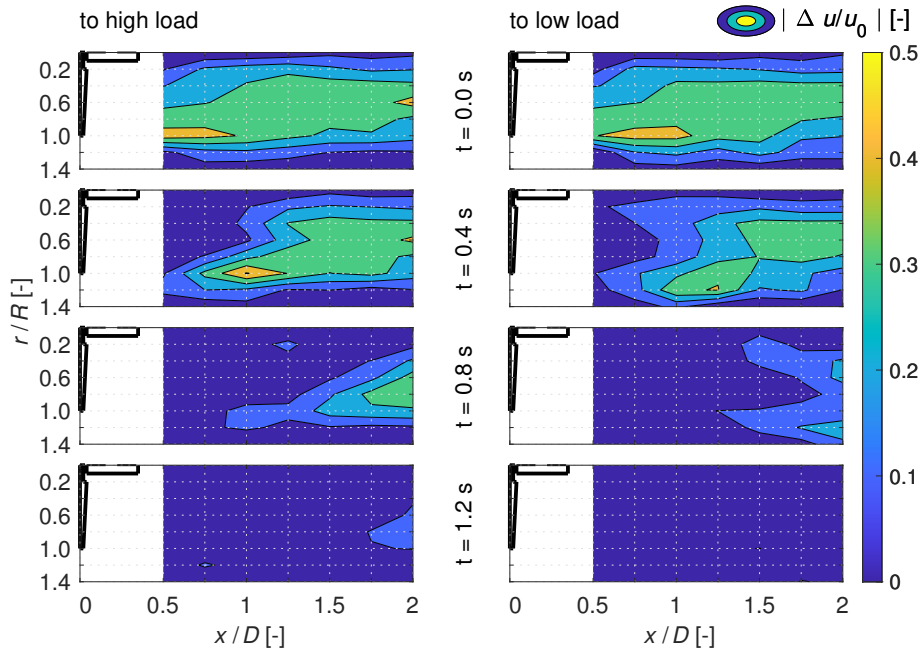
19

Figure 16. ~~Velocity~~ Top view on velocity contour in the horizontal plane at hub height of the difference to the new steady wake equilibrium at the four different time stamps, $0\,\mathrm{s}$, $0.4\,\mathrm{s}$, $0.8\,\mathrm{s}$ and $1.2\,\mathrm{s}$ after the pitch steps to high and to low load, normalised by the free stream velocity. The turbine dimensions are indicated in correct scale in the plots as a reference, with the x-axis being the axis of rotation.

Next, ~~we analysed~~ the deployment of the axial wake velocity as a response on the load steps is analysed. Six of the hot wire signals used to make the contour plot are plotted over time for the step to high load for the radii of $0.2\,R$, $0.6\,R$ and $1\,R$ at $0.5\,D$
385 and $1.5\,D$ distance behind the turbine are presented in Fig. 17.

~~The 1c model fit is applied to the hot wire signal. The fit does start at t_0, which is defined at the point where the velocity has adjusted by 28% to the new equilibrium. This definition is based on the mean value the axial inductions have adjusted during the pitch step.~~

For the radius at $0.6\,R$ a vertical line, called ~~wake ramp, is drawn at~~ a wake front, marks a characteristic t_1 of the exponential
390 decay, where the signal has adapted by 50% to the new equilibrium value. For the radius of $0.2\,R$ the velocity transient shows a local structure, where the velocity quickly decreases, increases again to subsequently decrease to the new equilibrium for both shown distances. The effect of the nacelle is assessed as unlikely to be the reason for this structure, as the nacelle only has a radius of $0.1\,R$. At the radius of $0.6\,R$ the signal decays exponentially. At $1\,R$ the signal increases quickly to a peak at nearly free stream velocity before decreasing exponentially to the new steady value. The signals at $0.5\,D$ behind the turbine for the
395 two higher radii, $0.6\,R$ and $1\,R$, show a better fit with the exponential decay function. For the farther distance at $1.5\,D$ the hot wire signals show an overshoot to lower velocities than the new equilibrium at around $1.5\,\mathrm{s}$ to $1.7\,\mathrm{s}$ for the two larger radii.

~~Further, we compared the fitted τ_{single} values for the wake flow measurements for both pitch directions. They are presented in Fig~~ The results for the indicated time constant fit are presented and discussed as an additional result in App. ~~C1. Spanwise~~
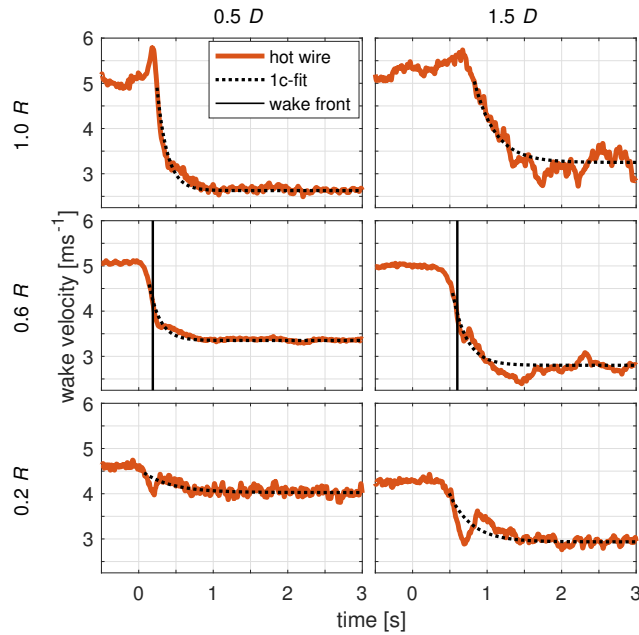
20

Figure 17. Ensemble averages of the axial wake velocity measured by hot wires for the three radii of $0.2\,R$, $0.6\,R$ and $1\,R$ at $0.5\,D$ and $1.5\,D$ distances behind the turbine for the step to high load.

400 ~~evolution of the axial wake velocity from $0.5\,D$ to $2\,D$ parametrized by the fitted time constant of the one time constant model for both pitch directions Between $0.5\,D$ and $1.5\,D$ no clear differences can be seen between pitch directions, apart from the root nearest radius of $0.2\,R$. The fitting of this radius is very sensitive due to the described local structure within the signal and should not be overinterpreted. For farther distances behind the turbine at $1.75\,D$ and $2\,D$ there is a clear difference between the pitch directions, with noticeable higher time constants for the step to high load for the radial range of $0.4\,R$ to $1\,R$, compared to both the time constants for the step in the same direction at rotor nearer distances and also in comparison to the step to low~~
405 ~~load at the same distances.~~ C.

In the next step, ~~we analyse the wake ramp velocity~~ the wake front velocity is analysed to measure how fast the transition point (the wake ~~ramp~~front) between the old wake and the new wake ~~does convect. We define it as the velocity this wake ramp travels~~ convects. This wake front can be thought of as being similar to a weather front. We define the wake front velocity by the time this characteristic wake front needs to travel from one considered downstream position to the next. So exemplarily
410 in Fig. 17 at $0.6\,R$ ~~we do have the wake ramp~~ there is the wake front for $0.5\,D$ at ~~$t_{\mathrm{ramp,0.5D}} = 0.20\,\mathrm{s}$~~ $t_{\mathrm{front,0.5D}} = 0.20\,\mathrm{s}$ and for $1.5\,D$ at ~~$t_{\mathrm{ramp,1.5D}} = 0.56\,\mathrm{s}$~~ $t_{\mathrm{front,1.5D}} = 0.56\,\mathrm{s}$. Within this time difference, the wake ~~ramp~~ front thus has travelled by $1\,D$, giving a mean wake ~~ramp~~ front velocity between these downstream distances.

In Fig. 18, this wake ~~ramp~~ front velocity is shown for both pitch directions, normalised by the free stream velocity. ~~Velocity of the wake ramp, defined by the mid point of the swept area weighted mean of the radii $0.4\,R$, $0.6\,R$ and $0.8\,R$, for both pitch~~
415 ~~directions, normalised by the free wind velocity. For orientation also the theoretical normalised wind velocity in the rotor plane~~

21

(1-a) and in far wake (1-2a), based on the measured thrust coefficient, are indicated for both steady states. The The wake front velocity is obtained by considering a mean value of the hot wire positions at the radii of $0.4\,R$, $0.6\,R$ and $0.8\,R$ were considered and a swept area-weighted mean, considering an annulus of . These signals were weighted based on their position with the conservation of mass in mind. For that each position was attributed an annulus reaching $\pm\,0.1\,R$ for each radius , was used . from the radius of the position. This mean velocity signal at the different downstream distances, which is used to obtain the wake front velocity, represents in this definition $(0.3\,R$ to $0.9\,R)$ the major part of the swept area of the rotor. Thus between
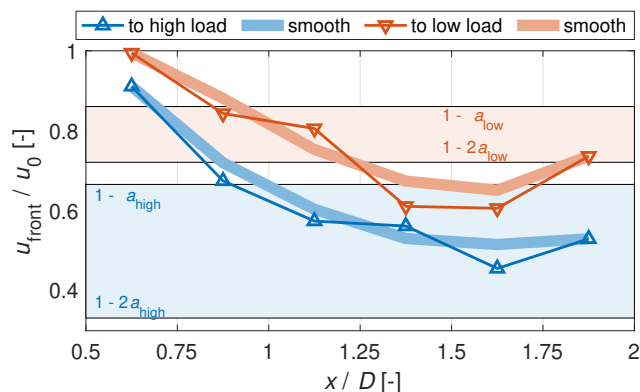

Figure 18. Velocity of the wake front for both pitch directions, normalised by the free wind velocity. For orientation also the theoretical normalised wind velocity in the rotor plane $(1-a)$ and in the far wake $(1-2a)$, based on the measured thrust coefficient, are indicated for both steady states.

every two considered downstream distances a mean velocity with which the wake ramp front moved can be calculated. Between the two nearest distances to the rotor, $0.5\,D$ and $0.75\,D$, the wake ramp front convects for both cases with $0.9\,u_0$ to u_0. This is faster than the expected velocity in the rotor plane for even the low loaded rotor. With increasing distance to the rotor for both cases the wake ramp front velocity decreases up to $1.5\,D$, whereas the velocity is higher for the step to low load. Based on this defined wake ramp front velocity the wake convection is on average 26% faster for the step to low load.

3.3 Loads results

Next, we compare the integral loads are compared as shown in Fig. 19. Two independent methods have been used. Once measured directly with strain gauges (SG) and once obtained indirectly from the LDA measurements in the rotor plane with the reconstruction procedure given in Sect 2.3 (LDA recon.). For the latter we distinguish it is distinguished between the use of the uA model and without it. For the strain gauge measurements additionally a version without the dynamic corrections for F_{thrust} and M_{aero} (SG no corr.) as introduced in Sect. 2.1.5 is presented to show the raw data. For the reconstructed loads further the influence of unsteady airfoil aerodynamics (uA) effects is shown around the overshoot, where it differs from the case without the uA model.
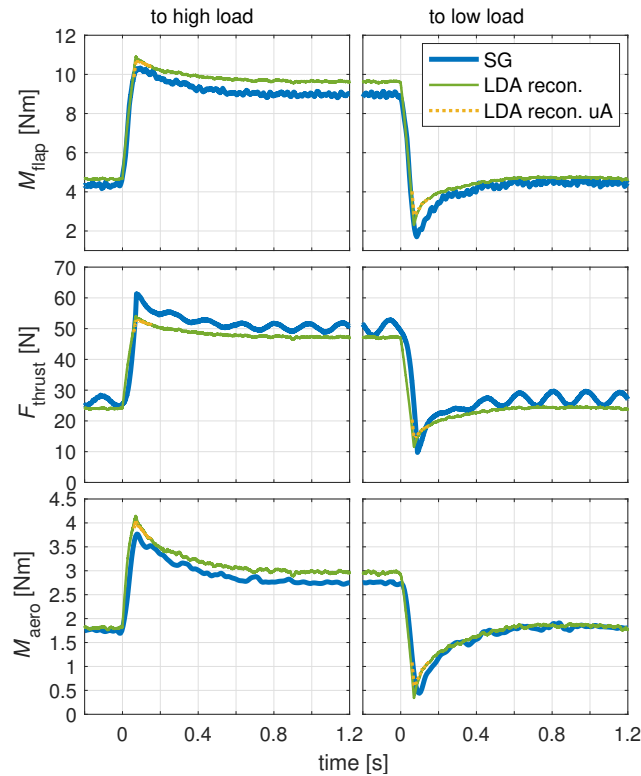
Figure 19. Integral turbine loads based on strain gauges with (SG) and without (SG no corr.) the dynamic corrections (as introduced in Sect. 2.1.5) and reconstructed loads based on Blade Element Theory from the LDA measurements without and with uA model.

435　Firstly, a clear overshooting behaviour of all load signals is apparent. Comparing the strain gauge measurements for M_{flap}, F_{thrust} and M_{aero} with the signals reconstructed from the LDA measurements indicate a good match of signals by means of steady values as well as the dynamic overshoot. Considering the uA model leads to a peak shaving of the overshoot. Also, the overshoot peak for the strain gauge signals, as well as for the reconstructed value with the uA model, are slightly shifted to higher t_0 values.

440　A more detailed comparison of the steady values at high and low load between the strain gauge measured integral loads and the reconstructed loads is plotted in Fig. 20, alongside the deviations of the reconstructed loads to the strain gauge measured loads. The two methods give similar load levels. Deviations differ between the load signals. The good agreement in terms of steady loads indicates good performance of this reconstruction approach with maximum deviations of 11%.

~~We attribute the~~

445　The slight overprediction of reconstructed loads for the M_{flap} and M_{aero} on the one hand and the underprediction of F_{thrust} ~~on a higher weighting of the higher radii~~~~for~~ is attributed to a higher influence of the larger radii. For the first two signals ~~than for the~~ the blade acts as a lever arm for the sectional forces, thus giving them a higher weighting. In contrast the sectional forces are added without considering a lever arm for F_{thrust}~~signal~~.
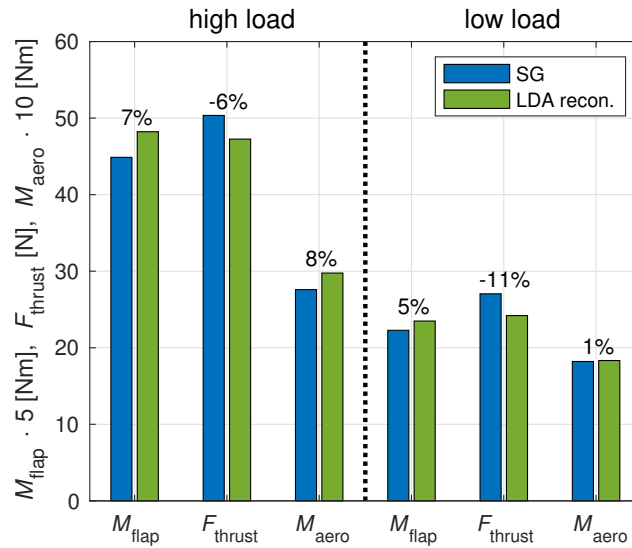
23

Figure 20. Comparison of the steady load levels for high and low load for the integral turbine loads M_{flap}, F_{thrust} and M_{aero} obtained by strain gauges and reconstructed from LDA measurements.

Further, the dynamics after the pitch step are compared. The amount of load overshoot, normalised by the difference between the steady values, is given for the load signals for both pitch directions in Fig. 21 a. The addition of the uA model reduces the
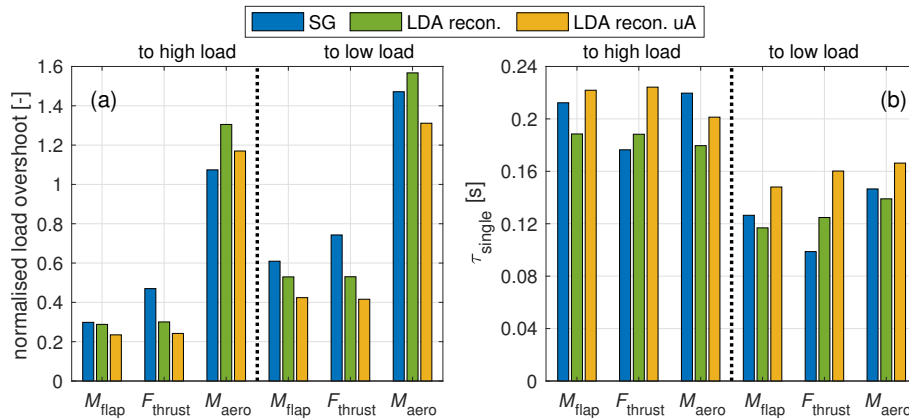

Figure 21. (a) Comparison of the amount of overshoot of the integral turbine loads M_{flap}, F_{thrust} and M_{aero}, obtained by strain gauges and reconstructed from LDA measurements without and with uA model for both pitch directions. (b) Comparison of the τ_{single} fit of the one time constant model to these integral loads.

450

amount of overshoot for all load channels. For M_{flap} the reconstructed loads provide a good fit, whereas the values with uA model show differences. High deviations are seen for F_{thrust} between strain gauge measurement and reconstructed loads,

24

especially with the uA model, but also without the model, for both pitch directions. The torque M_{aero} shows a good match with the reconstructed loads for both pitch directions.

455   The amount of overshoot is higher for the step to low load, when comparing the amount of overshoot between the two pitch directions per load channel and method. Based on the LDA reconstructed loads, which are not subject to dynamic corrections that might introduce errors, the normalised overshoot for the M_{flap} and F_{thrust} is similar per pitch direction, whereas the overshoot in M_{aero} is 3 to 4.5 times higher.

     The fitted values for the one time constant model to the integral loads is presented in Fig. 21 b for both pitch directions. The
460 time constants for all load signals and methods are longer for the step to high load than to low load. This is consistent to what was found in the velocity results before. The time constant is in general increased by including the uA model. For the step to high load M_{flap} and M_{aero} show a good match with the reconstructed uA method and an acceptable match for the step to low load. For F_{thrust} there are higher deviations between the strain gauge based time constant and the time constant based on the reconstructed uA load.

465   ~~The theoretical maximum overshoot~~ In order to assess the reasons for the differences in load overshoot it is of interest to investigate the theoretical maximum load overshoot when changing from one operational point to the other. This can be estimated based on the steady ~~induction measurements~~ states of the operational points and the theoretical dynamic maximum and minimum angle of attack distribution, as was ~~presented~~ introduced in Fig. 8~~, is investigated~~. The steady integral loads for high and low load are reconstructed as before for Fig. 19. ~~The maximum load overshoots are obtained by using~~ For the
470 maximum and minimum load the maximum and minimum dynamic angle of attack ~~distribution with the~~ distributions are used. The inflow to the segments is however defined by the inductions for the steady state just before the pitch step~~, so an~~. An infinitely fast pitch step is assumed~~and no~~, where the geometrical change of the blade pitch already happened, but the flow did not start to adapt. This apporach neglects uA effects that showed to reduce the overshoot~~, are considered~~. The derived theoretical maximum amount of overshoot based on the difference of maximum, respectively minimum load and the following
475 steady load is plotted in Fig. 22. A clear difference can be seen between the pitch directions for the axial loads M_{flap} and F_{thrust}, with about twice as high an amount of overshoot for the step to low load, than for the step to high load. For the torque the general trend is the same with 2.5 to 4.5 times the overshoot in comparison to the other signals. The trend is similar to the repeated LDA recon. values in the plot.

4   Discussion

480 In this section, the results for the inductions, wake flow and loads will be discussed. A focus for comparisons is on publications in connection to the NREL unsteady aerodynamics experiments phase VI (see Hand et al. (2001)), later referred to as just phase VI, as this experiment is the most widely studied dynamic inflow dataset so far.
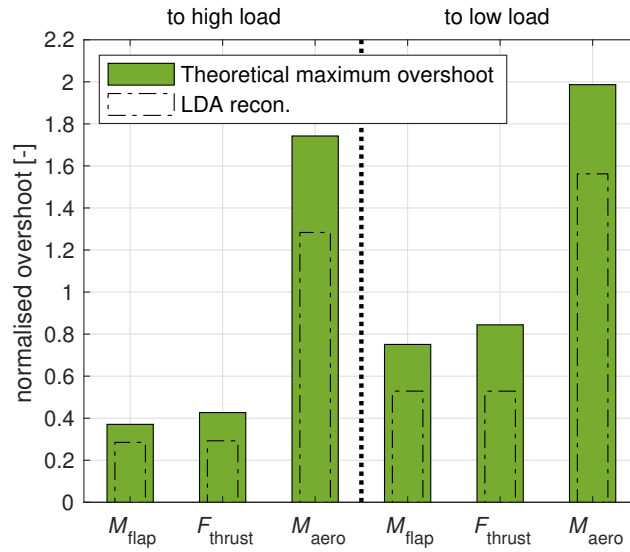
Figure 22. Theoretical dynamic overshoot for the step to high and low load for the integral turbine loads M_{flap}, F_{thrust} and M_{aero}, based on reconstruction from the LDA data, assuming an infinitely fast pitch step in comparison to the LDA recon. case from Fig. 21 a.

4.1 Inductions transients

Dynamic inflow phenomena on wind turbines were already indirectly shown in experiments based on integral loads for the
485   2 MW Tjæreborg turbine (see Øye (1991)), based on pressure sensor derived sectional forces on the phase VI (see Hand et al. (2001)) and MEXICO (see Boorsma et al. (2018)) model turbines and in the wake measurements behind an actuator disk with dynamic thrust changes (see Yu et al. (2017)). The presented axial induction transients in Fig. 9 based on the LDA measurements in the rotor plane are the first direct experimental evidence of dynamic inflow phenomena for wind turbines.

Pitch steps of the phase VI experiment were performed at $5\,\mathrm{m\,s^{-1}}$ wind speed and a tip speed ratio (TSR) of 7.5. The pitch
490   step of $15.9°$ took place during approximately 1/3 rotor revolution (pitch rate of $57°/\mathrm{s}$ over 0.28 s). This extreme pitch step is between a very highly loaded rotor at a rotor equivalent axial induction of 0.5 and 0 for the unloaded rotor. At the highly loaded rotor state, the turbine is in the turbulent wake state. This high induction state was later suspected to be responsible for problems in validation (Sørensen and Madsen (2006)).

Pitch steps in this paper were performed at $6.1\,\mathrm{m\,s^{-1}}$ and a TSR of 7.4. The pitch step of $5.9°$ was performed during
495   approximately 1/2 rotor revolution between rotor equivalent inductions of 0.34 and 0.14. The experiment thus is not operated in the turbulent wake state at the high load case.

The observed slight radial dependency for the single time constant (see Fig. 10), where the values slightly decrease towards the tip for the step to low load is in accordance with the observation by Schepers (2007) for the phase VI experiment, despite the more extreme change in rotor loading.

500   Pirrung and Madsen (2018) reproduced this behaviour for the phase VI experiment in a cylindrical wake model simulation. They explain this observation by the nature of the dynamic inflow process that cannot be described correctly by a one time constant model but by a two time constant model. They reason that the axial induction adapts by different amounts during the pitch step depending on pitch direction. This is governed by the wake velocity before the pitch step and thus influences the one time constant fit to the normal forces after the overshoot. In contrast, in the presented axial induction transients (see Fig. 9), ~~we~~

505   ~~see~~ it is seen that it adapts similarly during the pitch step for both pitch directions, by 28% on average.

    For the two time constant model fit to the axial wake inductions two variants, once with a freely fitted weighting ratio k_{free} and once with a prescribed weighting ratio k_{fix} of time constants, were shown in Fig. 11. Using k_{fix} allows for a direct comparison of τ_{fast} and τ_{slow} between the pitch directions. The radial dependency of τ_{fast}, with high values towards the root extends further into the blade for the step to low load. In their investigation of the normal force measurements on the phase

510   VI experiment, Sørensen and Madsen (2006) also saw this high τ_{fast} values at the root nearest radius of $0.3\,R$ for the step to low load, but not for the step to high load. In ~~our~~ the present and the phase VI experiment, this high τ_{fast} near the root is of the order of τ_{slow}. In ~~our~~ the present experiment, there is a ~~slight~~ difference in the τ_{fast} between pitch directions, with lower values for the step to low load from $0.5\,R$ to the tip. This difference between the pitch directions is not seen by Sørensen and Madsen (2006). Furthermore a radial dependance can also be seen from the mid of the blade towards the tip with an increase

515   for the step to high load (67%) and a slight decrease for the step to low load (-14%).

    For τ_{slow}, a very slight radial dependency can be seen for the fit with k_{fix}, with slightly increasing values (11%) towards the tip for the step to high load and slightly decreasing values (-16%) for the step to low load, similar to the fit of τ_{single}.

    The τ_{slow} values are on average about 28% faster for the step to low load, than for the step to high load. The same trend can be seen in Sørensen and Madsen (2006), however by a much higher value of around 100%. The likely explanation is the

520   higher difference in axial induction between the steady load levels for the phase VI experiment. Sørensen and Madsen (2006) and Pirrung and Madsen (2018) discuss this scaling of the time constants with the wake deficit and thus mean axial induction of the rotor. Also, the Øye dynamic inflow model (see Schepers and Snel (1995)) and other recent dynamic inflow models (e.g. Madsen et al. (2020)) use the axial induction to scale the time constants. There the fast time constant represents the near wake dynamics and decreases with radius and the slow time constant represents the far wake dynamics

525   Sørensen and Madsen (2006) and Pirrung and Madsen (2018) elaborated, based on measurements and simulations, that a two time constant model better describes the dynamic inflow process than a one time constant model. The two time constant approach also was implemented in the Øye dynamic inflow model (see Schepers and Snel (1995)). Yu et al. (2019) further showed, based on actuator disk vortex models, that a two time constant model describes the process better than a one or three time constant model. Comparing the fitting error of the 1c and 2c models to the axial wake induction measurements of ~~our~~

530   the present experiment (see Fig. 12), ~~we can verify this finding~~ this finding is verified based on the first direct meaurements of dynamic inflow phenomena. However, ~~we found~~ the root region ~~to be~~ is an exception, ~~where~~ as the process is defined by only one time constant.

The only minor differences in fitting error between the two variants with k_{free} and k_{fix} (see Fig. 11), illustrate the high sensitivity of the fitting process. Small changes in k have a noticeable impact on the τ_{fast} and τ_{slow} values, where one increases as the other decreases.

The overshooting behaviour of the tangential induction is a new finding. The time constants of the one time constant model have no clear radial dependency. They are lower for the step to low load and in general, slightly lower than those fitted for the axial induction. The overshoot also is more prominent for the step to low load. This behaviour is of interest for the physical understanding of the dynamic inflow effect, as the overshoot in the torque is directly counteracted by the change in wake rotation. We assume that the shed vortices due to the change in circulation introduce this instant overshoot in tangential induction. For the modelling of the dynamic inflow effect in BEM based codes, this behaviour is only of secondary interest, as the influence of the tangential induction on the angle of attack is negligible, apart from the blade root.

4.2 Wake evolution

~~We did not see a~~ No relevant influence of the shear layer between the open jet wind tunnel and the surrounding air is seen in the wake snapshots (see Fig. 15). On that basis, ~~we~~ it was decided to include these measurements in the paper. The main near wake and beginning far wake dynamics due to the pitch step should not be disturbed, despite the high blockage ratio of 0.28, as long as the wake and the shear layer of the open jet wind tunnel flow do not interact.

The velocity snapshots in the wake show differences in wake evolution between the pitch directions. The faster progression of the wake for the pitch step to low load, supports the presumption made by Schepers (2007) of different convection velocities of the wake consisting of the old vorticity and new vorticity, depending on the pitch direction. We assume the faster convection of this mixed wake for the case of the step to low load, starting with a low wake velocity pushed by a higher wake velocity to be the main driver of the faster time constants (τ_{single} and τ_{slow}) of the axial wake induction.

The dynamic widening of the wake after the pitch step to low load, as drawn in Fig. 15, is a new finding. We attribute it to the sudden change in trailed vorticity shed from the blade tip region. Part of the slow old wake is then pushed outboard by the fast new wake. The wake is not accelerated by the fast new wake at these larger radii, but by the even faster free stream wind velocity. This behaviour is a possible explanation for the decreasing time constants τ_{single}, respectively τ_{slow}, towards the tip for the pitch step to low load.

The overshoot in the velocity in the wake after a sudden change in thrust, as observed here for the radii at 1.0 R for the step to high load (see Fig. 17), has been discussed by Yu et al. (2017) based on wind tunnel experiments with a variable porosity actuator disk. They attribute these overshoots to the shed vorticity at the actuator disk edge due to the fast thrust change. The local structure at $0.2\,R$ where the root transition towards the axis of rotation starts, is opposite to the overshoot at $1\,R$ for the step to high load. We assume this to be the counterpart, the shed vorticity at the blade root, due to the sudden change in trailed vorticity. A connection of this shed root vortex to the radial dependency of τ_{fast} near the root cannot be concluded from the data but seems possible.

The quantitative comparison of the wake ~~ramp~~ front velocity (see Fig. 18), as a measure of the convection of the transition point between old and new wake, shows the faster velocity for the step to low load. On average, this wake convection velocity is 26% faster for the step to low load than for the step to high load. This difference resembles the difference in τ_{single} and τ_{slow} from the induction investigation in Sect. 4.1.

~~We see a~~ A fast initial wake ~~ramp velocity~~ front velocity is seen between $0.5\,D$ and $0.75\,D$, which is near the free stream velocity and higher for both cases than the expected axial wind velocity in the rotor plane for the low loaded rotor. An obvious explanation is that in the near wake, the dynamic inflow process of the whole rotor is governed by the influence of the trailed tip vortex, which does convect at similar velocities.

In the further course, the wake ~~ramp~~ front velocity slows down for both cases. For the step to low load, it even slows down between $1.25\,D$ and $1.75\,D$ to a lower value than the far wake velocity according to momentum theory for the new steady state. This behaviour can be explained by the mixed wake of both the old and new wake, which influence each other.

4.3 Load transients

The general comparison of the load signals obtained from strain gauges and reconstructed from the LDA measurements (see Fig. 19) shows a good agreement and thus proved the physical consistency of the induction measurements for these dynamic experimental cases.

For the steady equilibrium~~states, the quantitative~~, the comparison between the strain gauge measurements and the reconstructed loads (see Fig. 20) yields in generally good agreement, apart from the thrust at low load~~, which we suspect to be connected with the airfoil polars, especially at~~. Especially the here relevant high angle of attack region for the root airfoil is suspected to have uncertainties related to the low Reynolds number and possible laminar separation bubbles that can significantly increase the local lift.

For the flapwise blade root bending moment and the thrust, the load overshoot is much more pronounced for the step to low load than for the step to high load, whereas the trend for the torque is the same, but to a smaller extent. The magnitude of the overshoot depends on how much the axial induction has already adapted during the pitch process. As discussed in Sect. 4.1 they ~~adopt~~ adapt a similar amount during the pitch step for both pitch directions, so that this cannot explain the difference in overshoot between the pitch directions. The more pronounced overshoot of loads is also discussed for the phase VI measurements in Schepers (2007). He suspected the high angles in the stall region at the highly loaded rotor blade to be a possible reason for that phenomenon. In contrast, the high load case is operating safe outside of the stall regime for the experiment presented here, apart from the very root.

The higher relative overshoot of the torque by a factor of 3 to 4.5 compared to the flapwise blade root bending moment and the rotor thrust can be related to the lag in inflow angle and thus angle of attack behind the quasi-steady value. M_{flap} and F_{thrust} feel the effect mainly due to the change in the magnitude of the lift force, while M_{aero} feels the change in magnitude

and also the change of the projection of the lift force in the tangential direction due to the lag of the inflow angle (see Eq. 12). Because the F_thrust and mostly also M_flap are determined by the cosine of the inflow angle (see Eq. 11), the effect of the inflow angle lag is much smaller here.

The simplified approach to estimate the theoretical maximum overshoot for the load signals based on the steady inductions and the pitch angle change with the BET reconstruction (see Fig. 22), provides a solid reason for the different amount of load overshoot. It only depends on the turbine load characteristic, as the theoretical overshoot show a very similar ratio between load channels and pitch directions to the actual measured and reconstruceted load overshoot. The angle of attack overshoot for both pitch directions is the same in this mind experiment, however, near the high load the turbine reacts less sensitive on angle of attack changes than at the low load state.

Further, in the overshoot analysis (see Fig. 21 a) the large differences for the thrust between the strain gauge measurement and the reconstructed loads, both with and without the unsteady airfoil aerodynamics model, catches the eye. At closer investigation, the dynamic correction based on the estimated eigenfrequency and damping coefficient seems to be unsuited for very detailed comparisons. Therefore, this signal channel is omitted in the discussion of the detailed comparison. For the blade root bending moment and torque, the fit is good.

The 1c model investigation shows a good agreement between the strain gauge measurement derived and reconstruction based τ_{single} values. They are larger for the step to high load than for the step to low load, which is consistent with what was found before in the analysis of induction and wake results. They have a similar size to the fitted time constants to the axial inductions. The small changes in the overshoot of the reconstructed loads the uA model introduces demonstrate the sensitivity of the time constant fits to these small changes in the signal.

We do assume structural interactions Structural interactions are assumed to be the main driver for the observed differences in overshoot and also for the differences in the fitted time constants between the strain gauge signals and reconstructed loads with and without the uA model.

5 Conclusions

The objective of the presented dynamic inflow measurements was to deepen the general physical understanding of the dynamic inflow effect for wind turbines.

Direct experimental evidence of dynamic inflow is given through a very clear delay of induction factors at different radial positions at the rotor plane in response to a pitch angle step. Until now, dynamic inflow effects were only proven indirectly through measurements of turbine loads or flow measurements in the wake. We further It is affirmed that a two time constant model is more suited than a one time constant model to describe the behaviour of the axial induction for such a pitch step. The fast time constant of this model, representing the near wake influence, has a strong radial dependency near the root, however not and clear respectively slight dependency in the mid and tip region , where it approaches constant values towards the outer part of the bladefor the step to high, respectively low load. The slow time constant, related to the close far wake, shows a slight decrease towards the outer part for the step to low load and a slight increase for the step to high load. The overshooting

behaviour of the tangential induction is a novel finding of this work. It could be explained by the shed vorticity, which results from the circulation change during the pitch step. We expect that the radial dependency of the axial induction time constant is related to the observed dynamic wake expansion for the step to low load. With the wake measurement, ~~we~~ it is affirmed that the formation of the mixed wake after the pitch step convects faster for the step to low load, than for the step to high load. We suppose, that this is the reason for the lower slow time constants of the axial induction for the step to low load. ~~We further~~ It is found that the mixed wake after the pitch step initially travels at nearly free stream velocity for both pitch directions. We assume that the dynamic inflow effect in this near wake is governed by the ~~shed vortex from the tip~~ tip vortex due to the fast change in trailed vorticity. These vortices travel at such high velocities. Another finding is that the initial decay of the axial inductions during the pitch step is similar for both pitch directions. ~~We further identified~~ Furthermore, the aerodynamic characteristics of the turbine is identified to be the reason for the higher load overshoot for the pitch step to low load.

This comprehensive pitch step measurement set allows for detailed validation of engineering models and simulations for two relevant operational states, as we performed with the induction data in Berger et al. (2020).

Further investigations are recommended with ~~high fidelity~~ high-fidelity models of induction effects, eg. FVWM or Actuator Line CFD simulations to support the interpretation of the data ~~.~~ and improvement of models. Further planned steps to extend the understanding of the dynamic inflow process and enhance or develop models on the basis of this experimental setup are the generation of a wider database of pitch steps with varying parameters of inflow velocities, rotor speeds and rotor induction levels but also more realistic inflow conditions, including e.g. non-uniform inflow and gusts. With a wider database it can be tested if besides the axial induction, radial position and typical dynamic inflow time scaling factor $\frac{u_0}{R}$ further parameters have a significant influence on the time constants, as e.g. the operating TSR, background turbulence or non-uniform inflow. Due to the scaling of induction aerodynamics of this model turbine, based on the NREL 5MW turbine, the general behaviour of the induced velocities and wake are very similar to that turbine. It thus enables non-dimensional comparisons with that reference turbine, a turbine that has been extensively used worldwide in validation studies.

Data availability. Preprocessed data will be made publicly available with final publishing.

Appendix A: Counterbalance of the blade induction at the bisectrix between consecutive blades

The detailed derivation based on the theorem of Biot-Savart is given in Herráez et al. (2018) but the relevant formulas to produce the analytical solution in Fig. 5 a are given here.

Eq. (A11) of Herráez et al. (2018) is reproduced in Eq. (A1). The velocity induced by each of the N rotor blades (numbered $i \in [1, 2, .., N]$) is given in dependance of the azimuth angle of the blade ψ_i, the azimuth angle of the sampling point β and the

660　coordinates along the blade spanwise direction l. The circulation along the blade span is given by $\Gamma_i(l)$ and the azimuth angle of all blades can be defined by $\psi_i = \psi_1 + (i-1)\Delta\psi$, where $\Delta\psi = \frac{2\pi}{N}$.

$$u_i(r) = \frac{1}{4\pi} \int_0^R \Gamma_i(l) \frac{r\sin(\psi_i - \beta)}{[r^2 + l^2 - 2lr\cos(\psi_i - \beta)]^{\frac{3}{2}}} \, \mathrm{d}l \tag{A1}$$

Herráez et al. (2018) use a phase lock of the rotor for the simulations and compute the velocity along a circle for a specific radius. For the PIV validation in Herráez et al. (2018) and the application in this paper a stationary probe is used and the

665　rotor position is varied. The circulation $\Gamma_i(l)$ is obtained from the lift distribution calculated in Eq. 9 by the Kutta–Joukowski theorem.

The analytical solution of the axial probe $u_{probe,analytical}$ in Fig. 5 a considers an axial velocity of $u_{ax} = 4ms^{-1}$ and the combined effect of all three blades according to Eq. (A2). Note that the Eq. (A1) has a singularity for the probe position and a blade element being at the exact same position, that are excluded from the plot ($90°$, $210°$ and $330°$).

670　
$$u_{probe,analytical}(r) = \sum_{i=1}^N u_i(r) + u_{ax}(r) \tag{A2}$$

Appendix B: Unsteady aerodynamics model

The uA model as described in detail in Pirrung et al. (2017) Sect. 2.3 is reproduced with slightly altered variable names.

The model consists of two filter functions Eq. (B2, B3), which use the same time constant τ_{uA}^j, defined in Eq. (B1). The index j denotes the time step and the index QS the quasi-steady solution. The time step of the simulation, respectively reconstruction, is defined by Δt. The effective angle of attack α_{eff}^j, that indcludes the uA effect, is obtained by Eq. (B4).

675　
$$\tau_{uA}^j = \frac{c}{2u_{rel}^j} \tag{B1}$$

$$x_1^j = x_1^{j-1} \exp\left(-0.0455\frac{\Delta t}{\tau_{uA}^j}\right) + \frac{1}{2}\left(\alpha_{QS}^j + \alpha_{QS}^{j-1}\right) 0.165 u_{rel}^j \left(1 - \exp\left(-0.0455\frac{\Delta t}{\tau_{uA}^j}\right)\right) \tag{B2}$$

$$x_2^j = x_2^{j-1} \exp\left(-0.3\frac{\Delta t}{\tau_{uA}^j}\right) + \frac{1}{2}\left(\alpha_{QS}^j + \alpha_{QS}^{j-1}\right) 0.335 u_{rel}^j \left(1 - \exp\left(-0.3\frac{\Delta t}{\tau_{uA}^j}\right)\right) \tag{B3}$$

$$\alpha_{eff}^j = \frac{1}{2}\alpha_{QS}^j + \left(x_1^j + x_2^j\right)/u_{rel}^j \tag{B4}$$

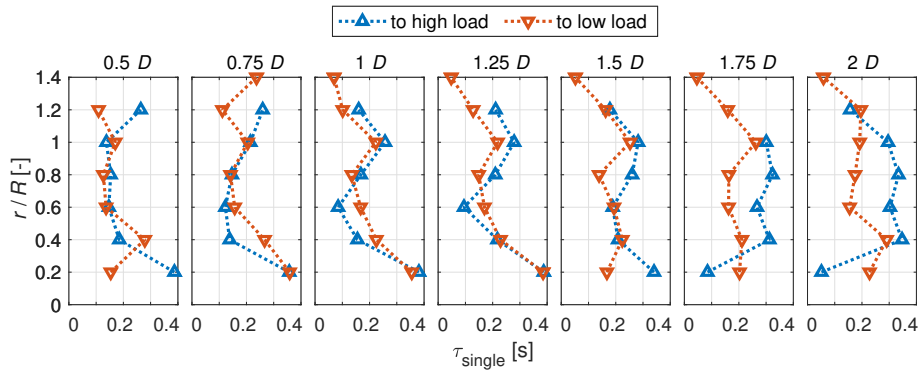680　**Appendix C: Time constant analyis of wake**

Figure C1. Spanwise evolvement of the axial wake velocity from $0.5\,D$ to $2\,D$ parametrized by the fitted time constant of the one time constant model for both pitch directions

The 1c model fit is applied to the hot wire signal shown in Fig. 17. The fit does start at t_0, which is defined at the point where the velocity has adjusted by $28\,\%$ to the new equilibrium. This definition is less accurate than the end of the pitch step, as for the axial induction transients. However no direct fitting start time can be defined and this value is based on the mean value the axial inductions have adjusted during the pitch step. The aim of this definition is to make the time constants comparable to these time constants of the axial wake induction.

Further the fitted τ_{single} values for the wake flow measurements are comparable for both pitch directions. They are presented in Fig. C1. Between $0.5\,D$ and $1.5\,D$ no clear differences can be seen between pitch directions, apart from the root nearest radius of $0.2\,R$. The fitting of this radius is very sensitive due to the described local structure within the signal and should not be overinterpreted. For farther distances behind the turbine at $1.75\,D$ and $2\,D$ there is a clear difference between the pitch directions, with noticeable higher time constants for the step to high load for the radial range of $0.4\,R$ to $1\,R$, compared to both the time constants for the step in the same direction at rotor nearer distances and also in comparison to the step to low load at the same distances.

In the actuator disk experiments by Yu et al. (2017) this trend also seems to be more prominent for the higher distances from the actuator disk.

Author contributions. FB designed, performed, processed and analysed the experiment and wrote the manuscript. DO assisted in the experiment, estimated steady corrections and wrote post processing scripts for the LDA data. JGS and MK contributed with several fruitful discussions from an early planning stage on. MK supervised the work. All co-authors thoroughly reviewed the manuscript.

Competing interests. The authors declare that they have no conflict of interest.

33

700

References

Berger, F. and Kühn, M.: Experimental investigation of dynamic inflow effects with a scaled wind turbine in a controlled wind tunnel environment, Journal of Physics: Conference Series, 1037, https://doi.org/10.1088/1742-6596/1037/5/052017, 2018.

705   Berger, F., Kröger, L., Onnen, D., Petrović, V., and Kühn, M.: Scaled wind turbine setup in a turbulent wind tunnel, Journal of Physics: Conference Series, 1104, 012 026, https://doi.org/10.1088/1742-6596/1104/1/012026, 2018.

Berger, F., Höning, L., Herráez, I., and Kühn, M.: Comparison of a radially resolved dynamic inflow pitch step experiment to mid-fidelity simulations and BEM, Journal of Physics: Conference Series, 1618, 052 055, https://doi.org/10.1088/1742-6596/1618/5/052055, 2020.

Boorsma, K., Schepers, J. G., Gomez-Iradi, S., Herraez, I., Lutz, T., Weihing, P., Oggiano, L., Pirrung, G., Madsen, H. A., Rahimi, H., and

710   Schaffarczyk, P.: Final report of IEA Task 29, Mexnext (Phase 3), Tech. Rep. ECN-E–18-003, 2018.

Drela, M.: XFoil: An Analysis and Design System for Low Reynolds Number Airfoils. Lecture Notes in Engineering, vol. 54, Springer Berlin Heidelberg, 1989.

Ferreira, C., Yu, W., Sala, A., and Viré, A.: Dynamic inflow model for a Floating Horizontal Axis Wind Turbine in surge motion, Wind Energy Science Discussions, https://doi.org/10.5194/wes-2021-34, 2021.

715   Hand, M. M., Simms, D. A., Fingersh, L. J., Jager, D. W., Cotrell, J. R., Schreck, S., and Larwood, S. M.: Unsteady Aerodynamics Experiment Phase VI: Wind Tunnel Test Configurations and Available Data Campaigns, Tech. Rep. NREL/TP–500–29955, 2001.

Hansen, M. H., Gaunaa, M., and Madsen, H. A.: A Beddoes-Leishman type dynamic stall model in state-space and indicial formulations, Tech. Rep. Risø-R-1354(EN), 2004.

Hansen, M. O. L.: Aerodynamics of Wind Turbines, Earthscan London, 2008.

720   Herráez, I., Daniele, E., and Schepers, J. G.: Extraction of the wake induction and angle of attack on rotating wind turbine blades from PIV and CFD results, Wind Energy Science, 3, 1–9, https://doi.org/10.5194/wes-3-1-2018, 2018.

Jonkman, J., Butterfield, S., Musial, W., and Scott, G.: Definition of a 5-MW Reference Wind Turbine for Offshore System Development, Tech. Rep. NREL/TP-500-38060, 2009.

Kröger, L., Frederik, J., Van Wingerden, J. W., Peinke, J., and Hölling, M.: Generation of user defined turbulent inflow conditions by an

725   active grid for validation experiments, Journal of Physics: Conference Series, 1037, https://doi.org/10.1088/1742-6596/1037/5/052002, 2018.

Madsen, H. A., Larsen, T. J., Pirrung, G. R., Li, A., and Zahle, F.: Implementation of the blade element momentum model on a polar grid and its aeroelastic load impact, Wind Energy Science, 5, 1–27, https://doi.org/10.5194/wes-5-1-2020, 2020.

Medici, D., Ivanell, S., Dahlberg, J.-Å., and Alfredsson, P. H.: The upstream flow of a wind turbine: blockage effect, Wind Energy, 14,

730   691–697, https://doi.org/10.1002/we.451, 2011.

Øye, S.: Tjæreborg Wind Turbine: 4. dynamic inflow measurement. Lyngby, Tech. rep., 1991.

Pirrung, G., Riziotis, V., Madsen, H., Hansen, M., and Kim, T.: Comparison of a coupled near- and far-wake model with a free-wake vortex code, Wind Energy Science, 2, 15–33, https://doi.org/10.5194/wes-2-15-2017, 2017.

Pirrung, G. R. and Madsen, H. A.: Dynamic inflow effects in measurements and high-fidelity computations, Wind Energy Science, 3, 545–

735   551, https://doi.org/10.5194/wes-3-545-2018, 2018.

Rahimi, H., Schepers, J. G., Shen, W. Z., García, N. R., Schneider, M. S., Micallef, D., Ferreira, C. J., Jost, E., Klein, L., and Herráez, I.: Evaluation of different methods for determining the angle of attack on wind turbine blades with CFD results under axial inflow conditions, Renewable Energy, 125, 866–876, https://doi.org/10.1016/j.renene.2018.03.018, 2018.

Ryi, J., Rhee, W., Chang Hwang, U., and Choi, J.-S.: Blockage effect correction for a scaled wind turbine rotor by using wind tunnel test data, Renewable Energy, 79, 227–235, https://doi.org/10.1016/j.renene.2014.11.057, 2015.

Schepers, J. and Snel, H.: Dynamic inflow: yawed conditions and partial span pitch control., Tech. Rep. ECN-C–95-056, 1995.

Schepers, J. G.: IEA Annex XX : Dynamic Inflow effects at fast pitching steps on a wind turbine placed in the NASA-Ames wind tunnel, Tech. Rep. ECN-E–07-085, 2007.

Schepers, J. G.: Engineering models in wind energy aerodynamics: Development, implementation and analysis using dedicated aerodynamic measurements, Ph.D. thesis, TU Delft, https://doi.org/https://doi.org/10.4233/uuid:92123c07-cc12-4945-973f-103bd744ec87, 2012.

Schepers, J. G. and Schreck, S. J.: Aerodynamic measurements on wind turbines, Wiley Interdisciplinary Reviews: Energy and Environment, https://doi.org/10.1002/wene.320, 2018.

Shen, W. Z. et al.: Tip loss corrections for wind turbine computations, Wind Energy, 8, 457–475, https://doi.org/10.1002/we.153, 2005.

Snel, H. and Schepers, J.: Joint investigation of dynamic inflow effects and implementation of an engineering method, Tech. Rep. ECN-C–94-107, 1995.

Snel, H., Houwink, R., Bosschers, J., Piers, W.J.; van Bussel, G., and Bruining, A.: Sectional prediction of 3-D effects for stalled flow on rotating blades and comparison with measurements, Tech. Rep. ECN-RX–93-028, 1993.

Sørensen, N. N. and Madsen, H. A.: Modelling of transient wind turbine loads during pitch motion, in: EWEC 2006, vol. 1, pp. 786–795, 2006.

van Engelen, T. G. and Hooft, E. L. V. D.: Dynamic inflow compensation for pitch controlled wind turbines, Tech. Rep. ECN-RX–04-129, 2004.

Vermeer, L., Sørensen, J., and Crespo, a.: Wind turbine wake aerodynamics, Progress in Aerospace Sciences, 39, 467–510, https://doi.org/10.1016/S0376-0421(03)00078-2, 2003.

Yu, W., Hong, V. W., Ferreira, C., and van Kuik, G. A. M.: Experimental analysis on the dynamic wake of an actuator disc undergoing transient loads, Experiments in Fluids, 58, 149, https://doi.org/10.1007/s00348-017-2432-9, 2017.

Yu, W., Tavernier, D., Ferreira, C., van Kuik, G. A., and Schepers, G.: New dynamic-inflow engineering models based on linear and nonlinear actuator disc vortex models, Wind Energy, 22, 1433–1450, https://doi.org/10.1002/we.2380, 2019.